Stacking of distributed dynamic strain reveals link between seismic velocity changes and the 2020 unrest in Reykjanes

Regina Maass[1,2,*], Sven Schippkus[1], Céline Hadziioannou[1], Benjamin Schwarz[3,4], Philippe Jousset[3], Charlotte Krawczyk[3,5]

Abstract

In this study, we measure seismic velocity variations during two cycles of crustal inflation and deflation in 2020 on the Reykjanes peninsula (SW Iceland) by applying coda wave interferometry to ambient noise recorded by distributed dynamic strain sensing (also called DAS). We present a new workflow based on spatial stacking of raw data prior to cross-correlation which substantially improves the spatial coherency and the time resolution of measurements. Using this approach, a strong correlation between velocity changes and ground deformation (in the vertical and horizontal direction) is revealed. Our findings may be related to the infiltration of volcanic fluids at shallow depths, even though the concurrent presence of various processes complicates the reliable attribution of observations to specific geological phenomena. Our work demonstrates how the spatial resolution of DAS can be exploited to enhance existing methodologies and overcome limitations inherent in conventional seismological datasets.

Preprint submitted to JGR: Solid Earth *April 5, 2024*

*Corresponding author
Email address: maass@cp.dias.ie (Regina Maass)
[1]University of Hamburg, Hamburg, Germany
[2]now at Dublin Institute for Advanced Studies, Dublin, Ireland
[3]GFZ German Research Centre for Geosciences, Potsdam, Germany
[4]Fraunhofer Institute for Wind Energy Systems IWES, Bremen, Germany
[5]Technical University Berlin, Berlin, Germany

Plain language summary

In 2020, an intense unrest period took place on the Reykjanes peninsula, in southwest Iceland, preceding the Fagradalsfjall volcano eruption in 2021. The unrest was characterized by ground movements of several centimeters (measured by GNSS stations) and accompanied by an increased number of local earthquakes. We investigate whether the unrest affects velocities of seismic waves that propagate through the crust in Reykjanes. Instead of conventional seismometers, we use seismic data recorded by a fiber optic cable. This technology has the advantage that measurements can be made every few meters along the cable. We exploit this high spatial sampling to improve methods traditionally applied to seismometer records. These improvements enable us to infer seismic velocity changes as a function of time and space along the fiber optic cable. We detect velocity changes that strongly correlate with the observed ground deformation in Reykjanes and are, therefore, likely linked to the unrest and/or its associated processes.

1. Introduction

Coda wave interferometry is a frequently used technique to detect structural and dynamic changes in the Earth's crust (e.g., Snieder et al., 2002; Grêt et al., 2006). This method is used to measure seismic wave velocities as a function of time. At first, measurements were applied to the coda of earthquake records, which constitute the long tail of phases following the earthquake signals (e.g., Chouet, 1979; Baisch and Bokelmann, 2001). Because coda waves experience multiple scattering, they have longer propagation paths in the Earth than direct waves. Thus, they are more sensitive to

changes in the subsurface (e.g., Snieder et al., 2002; Obermann et al., 2016; Martins et al., 2020; Toledo et al., 2022). However, monitoring requires that the sources are repeatable (e.g., Snieder and Hagerty, 2004; Hadziioannou et al., 2009). While active sources are perfectly repeatable but costly, earthquakes occur at irregular (mostly unpredictable) discrete points in time.

Information about Earth can also be extracted from ambient seismic noise, which is, for example, generated by ocean microseisms: Interactions between atmosphere, ocean gravity waves and the solid Earth continuously induce seismic energy (e.g., Longuet-Higgins, 1950; Hasselmann, 1963). Due to the continuity of the recordings, measurements of velocity variations at any time can be made. This has been exploited in a diverse range of research, including the monitoring of glaciers and landslides (e.g., Mainsant et al., 2012; Larose et al., 2015; Voisin et al., 2016; Guillemot et al., 2020; Bontemps et al., 2020), fault zones (e.g., Wegler and Sens-Schönfelder, 2007; Brenguier et al., 2008; Liu et al., 2018), volcano-related processes (e.g., Mordret et al., 2010; Sens-Schönfelder et al., 2014; Donaldson et al., 2017; Hirose et al., 2017), hydraulic systems (e.g., Hillers et al., 2014; Illien et al., 2022) and geothermal systems (e.g., Obermann et al., 2015; Sánchez-Pastor et al., 2019; Toledo et al., 2022). One drawback of these studies is that datasets consist of discrete points in space where seismic stations are deployed and therefore lack spatial density, such that detected velocity variations can only be attributed to large geographic areas between stations. This limits the ability to resolve small-scale responses of crustal rocks. Another limitation is that, in order to increase the signal-to-noise ratio (SNR) of data and obtain reliable measurements, data are usually stacked over time (e.g., Larose et al.,

2008). This makes the measurements less sensitive to short-term environmental processes.

Distributed dynamic strain sensing (also called DAS) is a technique that transforms an optical fiber into a dense array of strain sensors (e.g., Zhan, 2019; Lindsey and Martin, 2021). In multiple studies, it has been shown that DAS resolves structure and dynamics of the sub-surface at unprecedented spatial resolution and at low cost compared to conventional seismometers (e.g., Jousset et al., 2018; Lindsey et al., 2019; Zhan, 2019; Williams et al., 2019; Jousset et al., 2022; Diaz-Meza et al., 2023). In the context of ambient noise, DAS has been applied to obtain dispersion curves (e.g., Dou et al., 2017; Luo et al., 2020; Shao et al., 2022; Song et al., 2022; Zhou et al., 2022) and extract body waves through cross-correlation (Tonegawa et al., 2022). Velocity changes caused by ground water fluctuations were tracked along a DAS cable near the Sacramento river in the US (Rodríguez Tribaldos and Ajo-Franklin, 2021).

Our study focuses on the Reykjanes peninsula (SW Iceland), where an intense unrest period took place in 2020 in the area of the Svartsengi geothermal field (Figure 1). The unrest period consisted of three episodes of crustal inflation between January and August of 2020 and preceded a series of eruptions (Flovenz et al., 2022). Each inflation episode was followed by crustal deflation and associated with a large number of small to moderate earthquakes (M<4.8). Using ocean microseisms recorded by DAS, we measure seismic velocity changes in the crust beneath Reykjanes. Data come from the GFZ database (Jousset et al., 2020) and comprise 5.5 months between March and August of 2020, thereby covering two of the three inflation peri-

ods. The two questions driving our research are:

1. How can we exploit the spatial resolution of DAS to improve coda wave interferometry?

2. Do measurements of seismic velocity variations correlate with the deformation between March and August of 2020 or associated processes?

We address these questions by first applying the conventional workflow of coda wave interferometry (e.g., Brenguier et al., 2008; Steinmann et al., 2020) using single DAS channels in order to obtain measurements of velocity changes over time (Section 2). Then, we systematically investigate how the spatial resolution of DAS can be exploited to improve the temporal and spatial resolution of velocity changes (Sections 4 and 5). Finally, we interpret our results geologically (Section 6).

2. Data and Processing (conventional workflow)

The 21-km long fiber-optic cable is located on top of the mid-ocean ridge on the Reykjanes peninsula in the south-west of Iceland (Figure 1). The fiber was originally part of the telecommunication network in Reykjanes until it was repurposed as a strain sensor in seismological measurements (Jousset et al., 2018). Strain rate ($\delta\epsilon/\delta t$) records cover 164 days between March 1st and August 14th, 2020 (no data was provided on the 31th of each month) at a sampling rate of 1000 Hz, a channel spacing of 4 m and a gauge length of 10 m. During the measurements in 2020, the iDAS interrogator (Parker et al., 2014) was located in the town of Grindavik.

Because of computational constraints, we analyze a subset of the data, focusing on two 1.2 km-long sections of the fiber, each comprising approximately 300 channels (Figure 1). These sections, designated as SectionE (east) and SectionW (west) based on their geographical orientation, were selected because they are roughly co-linear on the DAS cable. This configuration is suitable for extracting stable Rayleigh waves through seismic interferometry, given that the Fresnel zones are sufficiently covered by ambient noise sources (e.g., Martin et al., 2021). Our objective is to measure velocity variations in the subsurface between SectionE and SectionW over time.

2.1. Pre-processing and cross-correlation

We process strain rate data with 24 hour long data segments. For computational efficiency, we decimate our data to a sampling rate of 5 Hz, which is in agreement with the frequency range of interest for our analysis. We subtract the mean and remove linear trends from the time series. We filter the data with a second-order zero-phase butterworth-bandpass filter retaining frequencies between 0.5 Hz and 0.9 Hz. This filter was chosen because frequencies higher than 0.9 Hz resulted in poor data quality and typical frequencies of the secondary microseisms (0.1 Hz - 0.4 Hz) could not be exploited due to the dominant impact of nearby isolated noise sources.

The core of the processing is cross-correlation of passive data recorded at different channels to extract empirical Green's functions between the channels, thereby turning one channel into a virtual source and the other channel into a receiver. This is also commonly referred to as ambient noise interferometry (e.g., Wapenaar et al., 2010). Prior to cross-correlation, we apply one-bit normalization (e.g., Bensen et al., 2007) by setting the amplitudes to

either -1 or 1 depending on their sign, in order to minimize spurious arrivals in empirical Green's functions due to more than 20,000 local earthquakes (Figure 9). We also apply spectral whitening using a running average ("rma") over 100 points within our cut-off frequencies 0.5 Hz and 0.9 Hz in order to reduce the influence of monochromatic signals in the cross-correlations (e.g., Bensen et al., 2007; Cupillard et al., 2011; Prieto et al., 2011). To start, we only include 28 channels from each section with an equidistant spacing of 40 m in the analysis (in total 56 channels). The reasoning behind this is to initially obtain results using the selected single traces. Later in this study, we will exploit the full spatial resolution of DAS and isolate the effect on the results when all 300 channels from each section are included in the analysis.

Throughout this work, channels on SectionE will be indexed with numbers 0-27, channels on SectionW with numbers 28-55 (Figure 2). We compute daily "intra-section" cross-correlations, thus cross-correlations between channels on SectionE and SectionW (e.g., cross-correlation of data recorded by channel 0 on SectionE and channel 34 on SectionW). Using this approach, we retrieve empirical Green's functions sampling the medium between the two sections.

2.2. Coda wave interferometry

To measure velocity variations over time, the stretching method is used (e.g., Lobkis and Weaver, 2003; Hadziioannou et al., 2011). This technique determines an optimal stretching factor ϵ that accounts for the degree of stretching or compression of a waveform relative to a reference waveform. The perturbation of the waveform is assumed to be linear $\tau = \epsilon t$, where τ is the arrival time of the wave in the altered and t in the reference medium

and ϵ quantifies the stretching or compression. Measurements are done on the coda waves that follow the direct surface waves in the retrieved Green's functions, because coda waves are particularly sensitive to changes in the medium. We define reference waveforms for each channel combination as the mean of daily cross-correlations over the entire time period (164 days). Perturbed (stretched or compressed) waveforms are defined as the mean over a shorter time interval in which a change of the medium properties is assumed to have happened. The determination of this time interval is presented in detail in Section 4 and leads to a value of 21 days. Thus, the measurement of velocity variation for a given channel combination and day d results from comparing the mean of 21 ($d - 10$ to $d + 10$) daily cross-correlations to the reference trace.

To quantify the stretching for a given perturbed waveform, a grid search is carried out. Perturbed waveforms are artificially stretched with a reasonable range of stretching parameters ϵ. For each ϵ, Pearson correlation coefficients (e.g., Hartung, 2009) are computed between the artificially stretched waveform and the reference trace for the coda wave time window. The stretching parameter that yields the highest correlation coefficient is linked to the relative velocity variation $\epsilon = -\frac{dV}{V}$. We define the coda window as the time period between 9 to 26 seconds following the direct surface waves arrival. The arrival time of the direct wave is estimated by dividing the distance between the virtual source and receiver by the velocity of the direct waves (determined through beamforming (Figure S1)). We perform the grid search in two steps: at first, we use a coarse grid and test 100 evenly spaced values between $\epsilon = -0.05$ and $\epsilon = 0.05$, corresponding to velocity changes between

-5% and 5%. This yields a first estimate of the optimal stretching parameter ϵ_{est}, or velocity change dVV_{est}, respectively. In a second step, the grid search is repeated but for a finer grid, including 100 evenly spaced values between $\epsilon_{est} - 0.002$ and $\epsilon_{est} + 0.002$ ($\mathrm{dVV}_{est} - 0.2$ % and $\mathrm{dVV}_{est} + 0.2$ %). For each combination of channels and day, this procedure is carried out separately on the acausal and causal part of the cross-correlations. To reduce instabilities in the results caused by, for example, an inhomogeneous source distribution, we stabilize measurements by averaging over the causal and acausal parts.

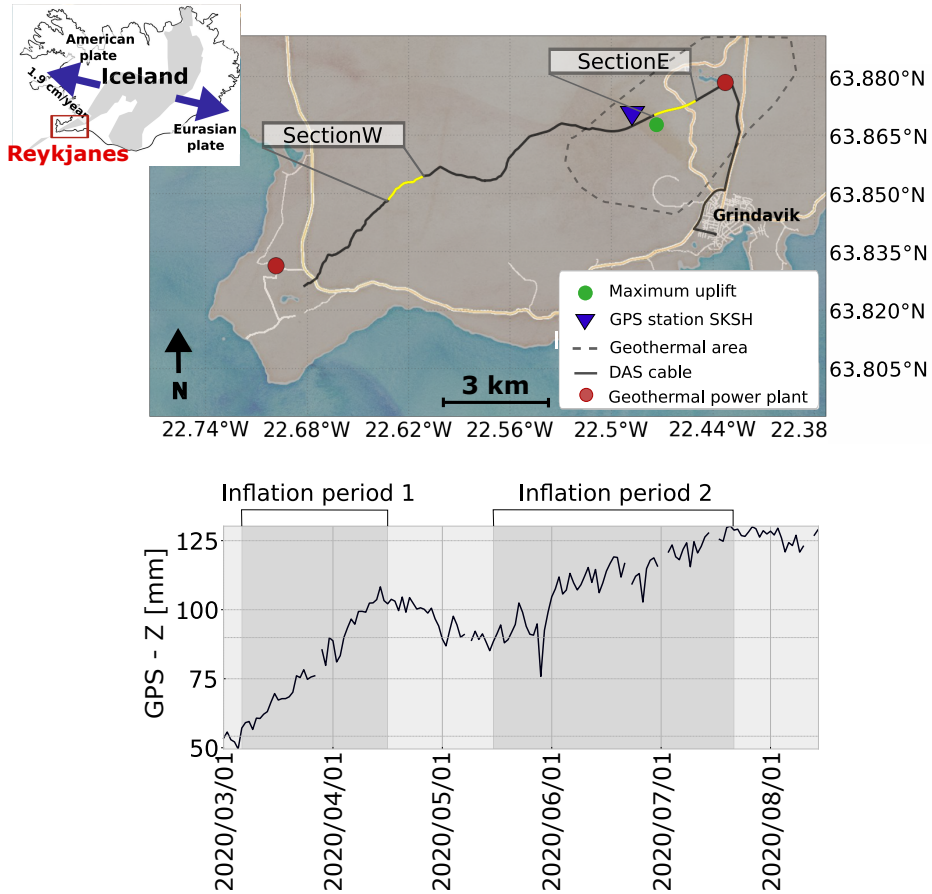

Figure 1: Top: The DAS cable is located at the south-western edge of the Reykjanes peninsula (red square in the small map of Iceland). The selected fiber sections (SectionE and SectionW), the approximate location of the Svartsengi geothermal area, GPS station SKSH and the point of maximum uplift are indicated. White and bright yellow lines represent roads. The centre of the deformation observed between March and August of 2020 coincides with the geothermal area. Bottom: Vertical ground displacement measured by GPS station SKSH. Outliers were removed prior to display. Two cycles of inflation and deflation (shaded in grey) were observed during our time period.

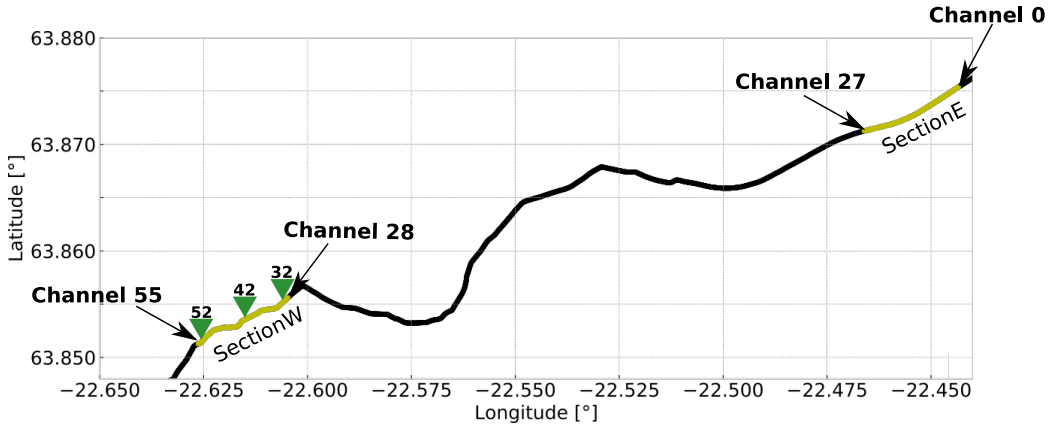

Figure 2: Selected fiber sections. Channels on SectionE are labelled with numbers 0-27, channels on SectionW with numbers 28-55. Positions of channels 32, 42, and 52 for which results will be shown are schematically indicated.

3. Exploiting the spatial resolution of DAS

Using beamforming techniques (Rost and Thomas, 2002), we estimate the apparent subsurface velocity of direct surface waves in our frequency range (0.5 - 0.9 Hz) to be 1.93 km/s (Figure S1). Thus, we expect apparent wavelengths between 2.14 km and 3.86 km in our data. Because these wavelengths are much larger than the channel spacing of 4 m, we assume that adjacent channels on the fiber record effectively the same waveform. This suggests that we can stack adjacent traces in space without introducing bias to the recorded wavefield, in order to increase the SNR of the data. In the context of ambient noise interferometry, spatial stacking of large-N arrays and DAS has been successfully applied to improve the stability of retrieved Green's functions, e.g., in order to reveal body waves in cross-correlations (e.g., Lin et al., 2013; Wang et al., 2014; Nakata et al., 2015; Tonegawa et al., 2022) and improve surface wave dispersion measurements (e.g., Shragge et al., 2021;

Czarny and Zhu, 2022; Li et al., 2022; Jousset et al., 2022; Cheng et al., 2023). It is important to emphasize that we measure velocity changes in the coda of cross-correlations. In contrast to direct waves, the coda resembles a diffuse wavefield constituting waves coming from all directions. This means that the conventional delay-and-sum approach (as used in beamforming) in which the SNR of a seismic phase can be boosted by time-shifting and stacking traces based on a specific slowness value and backazimuth, is not suitable for improving the SNR of coda waves. However, apparent wavelengths (2.14 km to 3.86 km) exceed the inter-station distance of 4 m by many orders of magnitude, which should allow us to simply stack traces in space without applying any time shifts. An unknown at this point is how many traces we can stack spatially without causing destructive interference of waveforms and corrupting the original coda wavefield. To answer this question, we carry out a synthetic study that is presented in the following section.

3.1. Synthetic parameter study

To investigate the question up to which spatial distance waveforms can be stacked, we use a synthetic approach rather than real data. This has the advantage that the results are not affected by poor data quality due to low SNRs or by strong amplitude variations caused by, for example, differences in the coupling of the fiber. We first create a harmonic wave propagating in the positive x-direction. The displacement u of the wave at position x_i with $i \in [0, 1, ...125]$ and time t is given by

$$
\begin{aligned}
u(x_i, t) &= \cos(kx_i - \omega t) + N(\sigma, x_i, t) \\
&= \cos\left(\frac{2\pi}{\lambda} x_i - 2\pi f t\right) + N(\sigma, x_i, t)
\end{aligned}
\tag{1}
$$

where λ is the wavelength, k the wave number, f represents the frequency and N denotes Gaussian random noise with standard deviation σ registering between 0.5 Hz and 0.9 Hz, since this is the frequency range of interest. We mimic our DAS cable and compute displacements for x-positions separated by 4 m, thus $[x_0 = 0, x_1 = 4, x_2 = 8, x_3 = 12, ..., x_{125} = 500]$ m.. We further simulate our real data setting by inserting $\lambda = 2.14$ km (previously determined with beamforming) and $f = 0.9$ Hz. For each position x_i we define a stack S as the mean of all traces trace between x_0 and x_i

$$
S(x_i, t) = \frac{1}{i+1} \sum_{j=0}^{i} u(x_j, t). \tag{2}
$$

This is equal to averaging over a spatial distance $x_i - x_0$. Figure 3 illustrates this procedure. In order to quantify the alteration of the waveform due to spatial stacking, we compute Pearson correlation coefficients between the stacks and the initial waveform $u(x_0, t)$ at all positions x_i, i.e. for increasing spatial stack lengths $L \in [0, 4, 8, ...500]$ m. We also investigate the dependency on the noise level, which is defined by the standard deviation $\sigma \in [0, 0.2, 0.4, ..., 10]$ of the Gaussian noise distribution. Results are shown in Figure 4. The longer the stack length and the higher the noise level, the smaller the correlation coefficients. Thus, the optimal spatial stack length for a given wavelength and frequency is controlled by the degree of random

noise in the data. We define a threshold at a stack length of $L = 200\,\mathrm{m}$, which corresponds to 50 adjacent traces on the DAS cable. Depending on the level of random noise, correlation coefficients between <0.80 and 0.95 are expected for this stack length. Assuming low noise levels, these correlation coefficients seem high enough to guarantee that no bias is caused to the original wavefield.

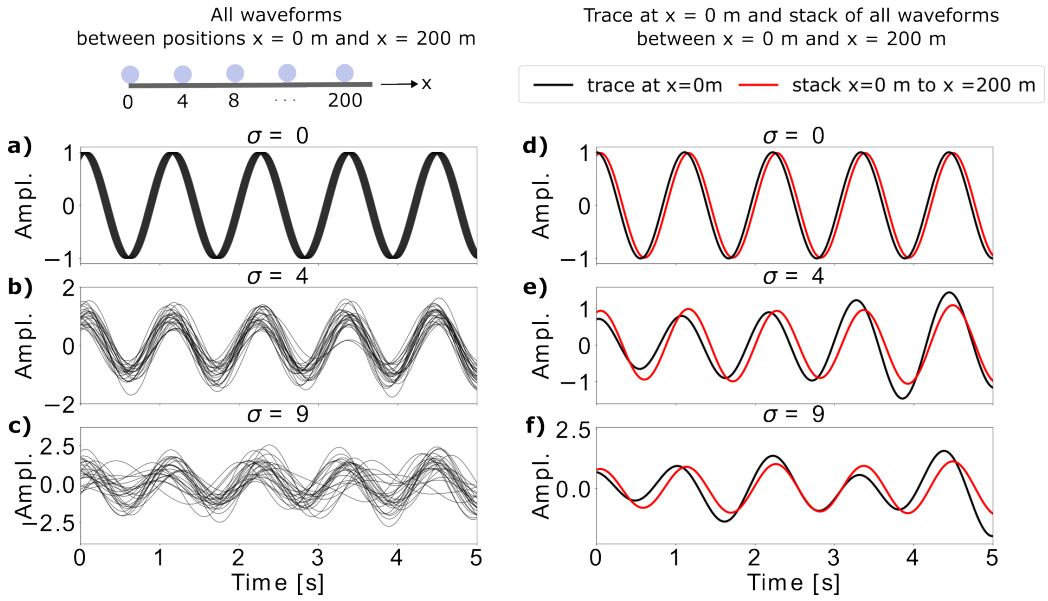

Figure 3: a-c) Time series $u(x_i, t)$ at positions $[x_0 = 0, x_1 = 4, x_2 = 8, x_3 = 12, ..., x_{50} = 200]$ m due to a harmonic wave travelling in the positive x-direction. Three different noise levels in a) $\sigma = 0$ (no noise), b) $\sigma = 4$ and c) $\sigma = 9$ are considered. d-f) Stack $S(x_{50}, t)$ (mean of all times series u between $x_0 = 0$ m and $x_{50} = 200$ m) is plotted together with the waveform $u(x_0, t)$ for three different noise levels in d) $\sigma = 0$ (no noise), e) $\sigma = 4$ and f) $\sigma = 9$. For example, the stack shown in e) is the mean of all traces shown in b).

3.2. New workflow based on spatial stacking of DAS data

Using the results from the synthetic study that was presented in the previous section, we carry out spatial stacking with the decimated data before

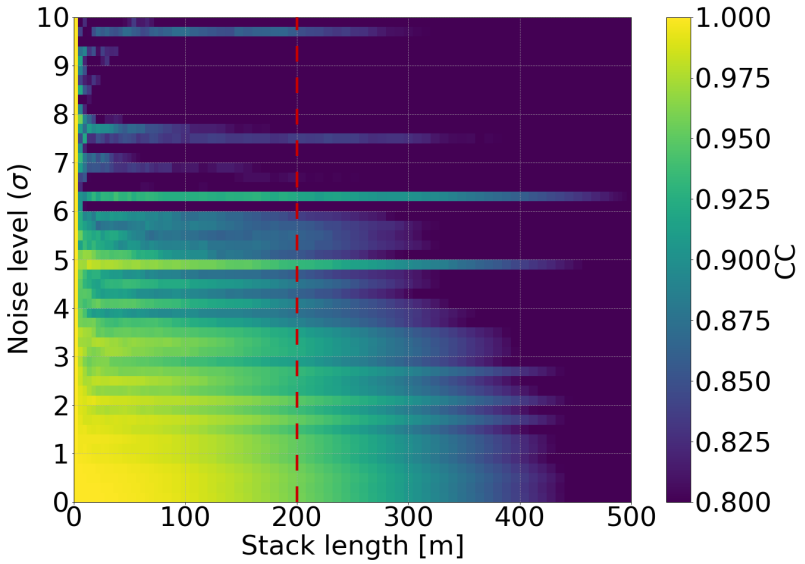

Figure 4: Correlation coefficients CC between the stacked waveforms $S(x_i, t)$ and the initial waveform $u(x_0, t)$ at $x_0 = 0\,\mathrm{m}$. The optimal spatial stack length L for a given frequency and wavelength depends on the degree of random noise contained in the data. At a stack length of $L = 200\,\mathrm{m}$ (red dashed line), correlation coefficients of approximately 0.95 are expected for low noise levels.

any further pre-processing or cross-correlation is applied. In order to systematically investigate the effect that spatial stacking has on the results, we test different values $L \in [24, 48, 96, 144, 200]$ m. Thus, we generate 5 additional sub-datasets based on different spatial stack lengths. Table 1 summarizes the properties of each sub-dataset. Stacks are computed via

$$u_L(x_k, t) = \frac{1}{N+1} \sum_{l=k-\frac{N}{2}}^{l=k+\frac{N}{2}} u(x_l, t) \tag{3}$$

where $u(x_k, t)$ is the recorded strain rate at time t and position x_k with $k \in [1, 2, ...300]$ (300 channels on each section). Hence, each stack is the mean of $N+1$ traces, separated by 4 m, with central position x_k. We evaluate this

formula for all previously selected channels $j \in [0, 1, ..., 55]$ on SectionE and SectionW (see Section 2). For each sub-dataset, we perform the processing steps described in Section 2.

Sub-dataset	L [m]	N	Percentage of smallest wavelength
Single traces	0	0	0
1	24	6	1.1
2	48	12	2.2
3	96	24	4.5
4	144	36	6.7
5	200	50	9.3

Table 1: Properties of each sub-dataset. In addition to the single traces for which no spatial stacking was applied, we generate 5 datasets based on different spatial stack lengths L (or the number of stacked DAS channels $N + 1$, respectively). The maximum spatial stack length $L = 200\,\text{m}$ corresponds to 9.3% of the smallest dominant wavelength (2.14 km) in our data.

4. Improving temporal resolution

The stretching method was introduced earlier in this work and quantifies the degree of stretching or compression of a perturbed waveform relative to a reference waveform. Perturbed waveforms are thereby defined as the mean of traces over a certain time interval $T_s + 1$. A very low T_s (short time interval) implies a high time resolution but also low signal-to-noise ratios (SNRs) which can introduce bias to the measurements and lead to unreliable results. A very large T_s (long time interval) lowers the time resolution of

measurements, smearing out short-term environmental processes of interest. To define T_s, we examine two parameters: For an increasing temporal stack length, we evaluate i) the Pearson correlation coefficient and ii) the SNR between stacked cross-correlations and reference traces. The SNR is defined as the fraction of the maximum amplitude of the coda window (picked between 9 and 26 seconds after the direct surface wave arrival) and the standard deviation of the noise window (a 16 seconds long time window at the tail of cross-correlations). Figure 5 shows the result for a selected channel combination. The larger the number of stacked daily cross-correlations, the higher the correlation coefficients and SNRs. The optimal temporal stack length T_s is chosen where correlation coefficients converge towards a value of 1 (reach a stable plateau), given that SNRs show a robust evolution in time (e.g., Larose et al., 2008; Steinmann et al., 2020). Following this, we set $T_s = 20$ days. It is apparent that this value depends on the spatial stack length L. For instance, with single traces and a short spatial stack length of $L = 24\,\mathrm{m}$, correlation coefficients have not yet stabilized at the chosen value of $T_s = 20$ days, indicating that a higher T_s might be more appropriate to obtain reliable results. Conversely, with $L = 200\,\mathrm{m}$, an even shorter T_s would suffice. This is a valuable result: stacking raw data in space before cross-correlation enhances time resolution in coda wave interferometry. The larger the spatial stack length, the higher SNRs and the faster the convergence of correlation coefficients. However, in all following analyses, we maintain $T_s = 20$ days across all spatial stack lengths to isolate the impact spatial stacking has on the results.

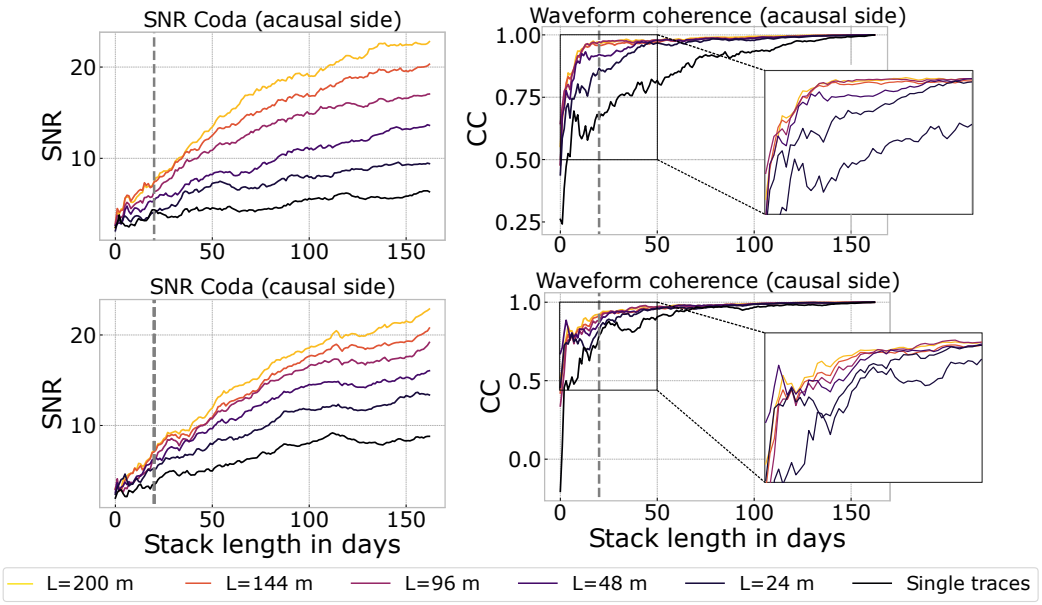

Figure 5: SNR and waveform coherency (correlation coefficients CC between the reference waveform and temporally stacked cross-correlations) for an increasing stack length in days (channel combination 3_42). Results for both the causal and acausal side of the cross-correlations are shown. The larger the spatial stack length L, the higher the SNRs and the faster the convergence of correlation coefficients. The dashed grey lines at $T_s = 20$ mark the temporal stack length chosen for our analysis.

5. Results - velocity changes

5.1. Visualization

Our goal is to spatially and temporally resolve processes related to the deformation. The area affected by the ground deformation as observed in GNSS data matches the area of the geothermal field, and thus covers DAS channels on SectionE (Figure 1). We therefore present our results as follows: We select a reference channel on SectionW and plot results for all combinations of stations on SectionE and the selected channel in 2-dimensional "gathers" (e.g., Figure 6). Using this approach, we track spatio-temporal changes in seismic velocities along SectionE relative to a fixed reference point on SectionW.

Throughout this work, we will present results from three reference channels (32, 42, 52), situated respectively at the eastern end, in the middle, and at the western end of SectionW, to illustrate the range of outcomes across the entire section (Figure 2).

5.2. Effect of the spatial stack length

Figure 6 shows results for reference channel 42 on SectionW. In the case of the single traces, velocity variations look rather randomly distributed, although spatial coherency in some places can be suspected, for example in July. Correlation coefficients vary; at the beginning of May, June and July, particularly low values are measured. For a stack length of $L = 24\,\mathrm{m}$ (1.1 % of the smallest dominant wavelength), the spatial and temporal coherency is considerably improved. Overall, larger correlation coefficients are measured. Areas of decreased and increased wave speeds can be more clearly distinguished and trends start to emerge in the results. Outliers, i.e., particularly strong deviations represented by oversaturated colors, are reduced in number. The spatial and temporal coherency of velocity changes further improves with each increase in L, accompanied by growing correlation coefficients. Trends in the data stabilize, allowing a clear spatio-temporal pattern of velocity changes to be observed: an area of increased wave speed is revealed and the end of March and April that is first detected by channels in the north-east of SectionE and, as time passes, by channels in the south-west. The same trend can be observed at the beginning of June and July. In between those time periods, lower than average velocities are measured. Finally, for $L = 200\,\mathrm{m}$ (9.3 % of the smallest dominant wavelength) the highest spatio-temporal coherence and largest correlation coefficients are obtained.

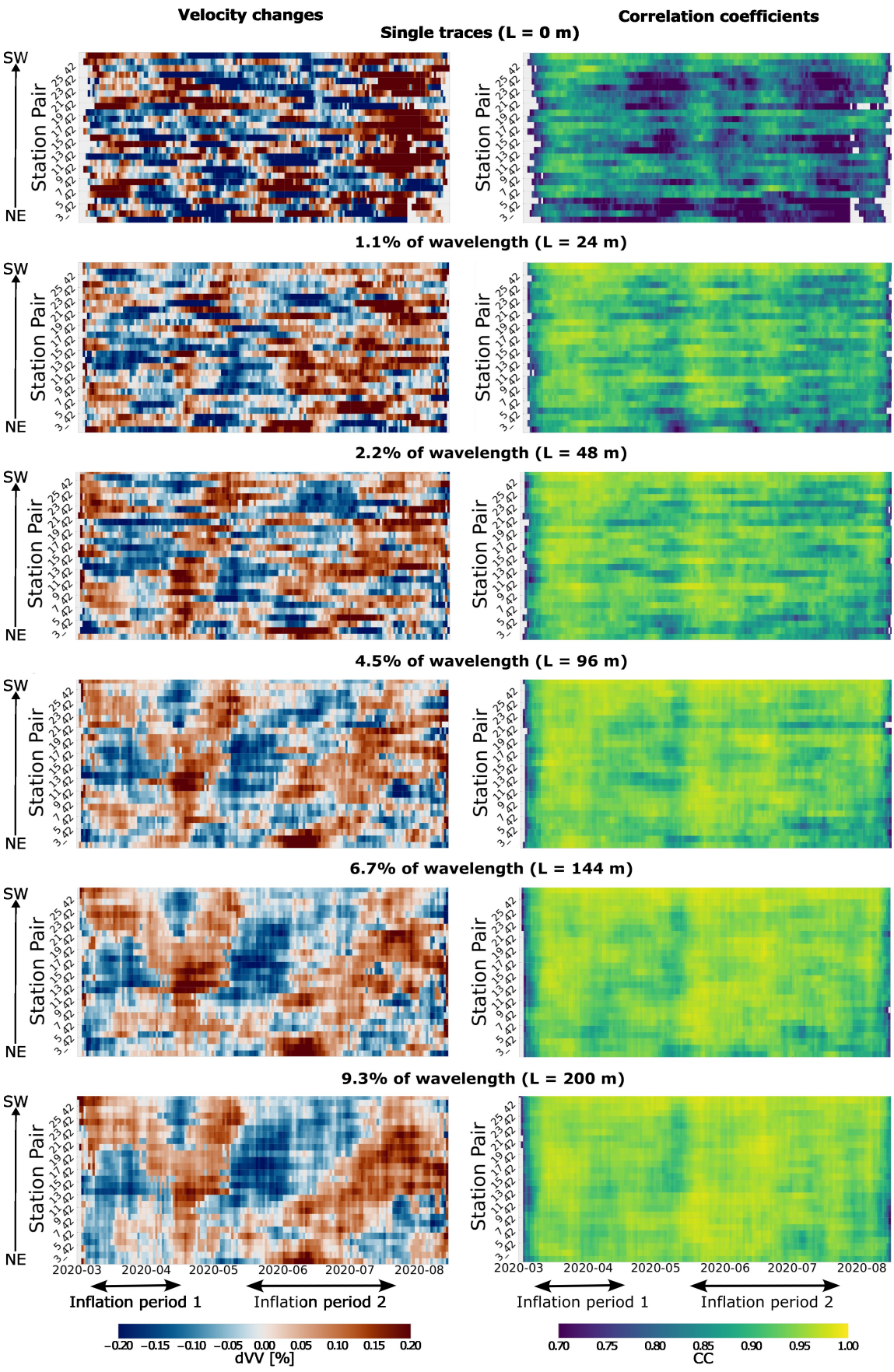

Figure 6: Gathers for an increasing spatial stack length L (reference channel 42). Correlation coefficients (CC) with values < 0.7 and their corresponding velocity changes (dVV) are not displayed. Results for the easternmost station are shown at the bottom, results for the westernmost station on SectionE are displayed at the top of each gather. Thus, by going from the bottom to the top along the y-axis, we move from the north-east to the south-west along SectionE (see also Figure 2). Inflation periods are marked with horizontal arrows below the time axis. With each increase of L, CCs are higher and the spatial and temporal coherency of velocity variations is improved.

Results for reference channels 32 and 52 (Figures S2 and S3) underscore the improving spatio-temporal coherency in the results as the spatial stack length increases.

5.3. Spatio-temporal variability and evolution

Results differ slightly depending on which reference channel is chosen on SectionW (Figure 7a-c)). For example, stations 19-27 on SectionE in combination with reference channel 42 measure increased velocities in March, but lower velocities in combination with reference channel 52 (dotted squares in Figure 7b and c). These differences may be due to local effects beneath the channels on SectionW, such as the coupling of the fiber and local geology. Thus, differences in the results reveal valuable information about the subsurface near the reference channels. The main trends, that is, time periods and areas of decreased and increased wave speeds are, however, similar for all reference channels. To quantify the main trends and in order to isolate processes that happen beneath SectionE, we smooth out local effects at SectionW and compute an average by stacking all (twenty-eight) gathers. The result is shown in Figure 7d). Overall, velocities drop at the beginning of the first inflation period. This is followed by a velocity increase (feature **1** in Figure 7d) until they reach a local maximum at the beginning of the first deflation period with higher than average values. From there, seismic wave speeds decrease until they reach a local minimum at the beginning of the second inflation period. This is again followed by a velocity increase as the second inflation period goes on (feature **2**). Striking is that velocity changes tend to be first measured by channels in the north-east, and then, as time passes, by channels in the south-west of SectionE. For example, higher than

average wave speeds are measured by channels in the north-east at the end of the first and during the second inflation period (features **A** and **B** in Figure 7d)). The time at which these increased velocities are picked up by the westernmost channel coincides with periods of crustal deflation. This channel is very close to the point at which the maximum uplift in the area was observed (Figure 1).

6. Discussion

6.1. Smoothing effect due to spatial stacking

In order to improve SNRs of data in the context of coda wave interferometry, temporal stacking is usually applied which comes at the expense of time resolution. With spatial stacking, DAS provides another option to improve SNRs which compensates for temporal stacking (Figure 5). Similar to temporal stacking, there is a smoothing effect as we average over a spatial distance and may thus blur out localized velocity variations on individual channels. In return, however, we achieve a time resolution that allows us to capture short-term deformation cycles over a relatively short total time period of 5.5 months (Figures 6 and 7). In general, the extent to which spatial stacking is beneficial depends on the specific objectives of the study. Nevertheless, we note that while spatial stacking may smooth out local velocity changes, typical seismological datasets inherently lack sufficient spatial resolution at the meter-scale to capture such nuances. We further introduce a smoothing effect by selecting every 10th channel along the fiber sections with a 40-meter separation as virtual source/receiver, and gradually extending the spatial stack length from 24 m to 200 m. This is because for spatial

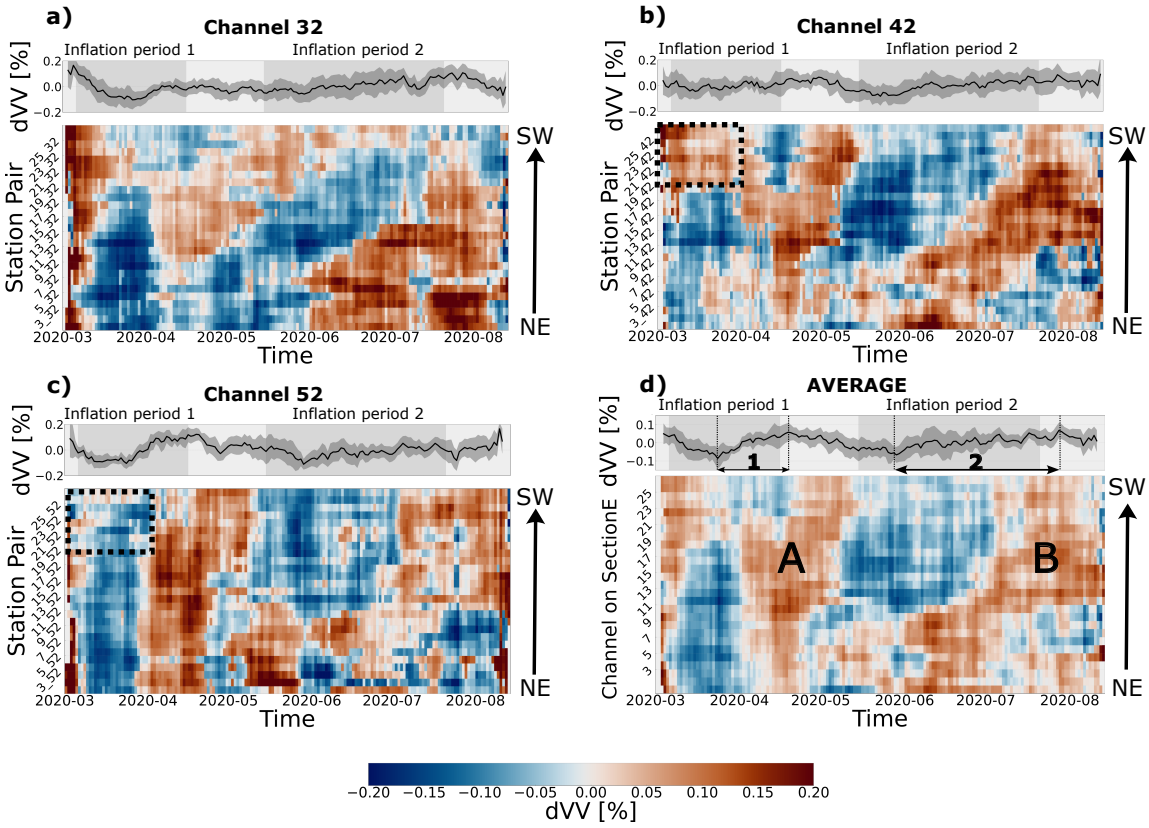

Figure 7: a-c) Gathers for reference stations 32, 42, 52 (see Figure 2 for the station locations). The easternmost station on SectionE is displayed at the bottom, the westernmost station on SectionE is shown at the top of the gathers as described in Figure 6 and indicated with the arrows. Results for a spatial stack length $L = 200\,\mathrm{m}$ are shown. Above each gather, the spatial averages (mean over all station pairs) are plotted with standard deviations. Inflation periods are shaded with grey color. The black dotted squares in b) and c) indicate an area for which different results were obtained for reference channels 42 and 52 (see text). d) Average over all (twenty-eight) gathers. Velocity changes tend to be first picked up by channels in north-east and later in the south-west of SectionE.

stack lengths $L >= 48\,\mathrm{m}$, virtual sources overlap (multiple virtual sources are included in the stacks). Such smoothing effects are inherent in distributed dynamic strain sensing (DAS) due to the gauge length typically exceeding the channel spacing. Our method can be seen as a systematic expansion of the gauge length up to a predetermined threshold (defined through the synthetic

parameter study) that ensures preservation of the original coda wavefield.

6.2. Bias introduced by spatial stacking and synthetic parameter study

It is important to discuss whether spatial stacking could introduce bias by causing an apparent stretching of the waveforms. This scenario may occur, for instance, if the distribution of the noise source is not uniform, as we illustrate through the following line of thought: if the position of the noise source changes over time, the radiation pattern at the virtual source, changes. Through cross-correlation, a different part of the Earth's crust may be emphasized, potentially resulting in different incident angles of the wavefront arriving at the receivers. This may cause that a different fraction of the (apparent) wavelength is stacked on one day compared to another day and introduce an apparent stretching. However, how variations of the noise source distribution affect the coda of cross-correlations, is generally a matter of debate (e.g., Froment et al., 2010; Colombi et al., 2014). Recent research indicates that coda waveforms may be dominated by isolated noise sources continuously activated at specific locations, rather than by fully scattered waves (Schippkus et al., 2023). This means that isolated noise sources may contribute to velocity changes identified with the stretching method, questioning the common assumption that measurements of velocity changes on coda waves originate in structural and dynamic changes in the subsurface only. Further analyses will help to identify potential pitfalls of spatial stacking in the context of coda wave interferometry, similar to the synthetic study presented in this paper. This parameter study is founded on several assumptions: the assumption of Gaussian random noise, considered independent across the channels, is a simplification. In reality this unwanted noise

might be coherent across multiple channels and get enhanced through spatial stacking. Similarly, we assume that no local or isolated ambient noise sources are present that introduce spurious arrivals prone to amplification. Hence, analogous assumptions to those commonly employed in ambient noise interferometry are made, wherein the synthetic parameter study mirrors the ideal scenario of a homogeneous and non-variable noise source distribution. Nevertheless, it serves as an initial framework upon which further numerical simulations and synthetic examples can build.

6.3. Discrepancy between causal and acausal side

We averaged over causal (positive) and acausal (negative) sides of cross-correlations. This is usually done in order to account for instabilities due to, for example, an inhomogeneous noise source distribution. Provided that the wavefield is fully scattered, we expect similar measurements on both sides of the correlations. However, different, but spatially coherent results are obtained for the causal and acausal parts, as demonstrated in Figure 8. Measurements on the acausal sides are smaller in magnitude and tend to show the opposite trend compared to the causal side. Weemstra et al. (2016) apply coda wave interferometry in our study region using ambient seismic noise. They use a very similar processing scheme and measure contradicting stretching values on the causal and acausal sides for similar frequencies (0.5 - 1 Hz). The authors argue that this may be associated with a variable distribution of noise sources. Reykjanes is located at the south-western edge of Iceland such that the noise sources in the Atlantic ocean likely are in close proximity to the stations. A change in the noise sources thus has a greater impact on the measurements. Our observations suggest that the noise source

446 distribution affects our measurements and that the wavefield is not entirely
447 diffuse. This implies that measurements may not be solely attributable to
448 structural changes in the crust. Still, we observe a compelling correlation
449 between geological processes and our measurements, which we discuss in the
450 following.

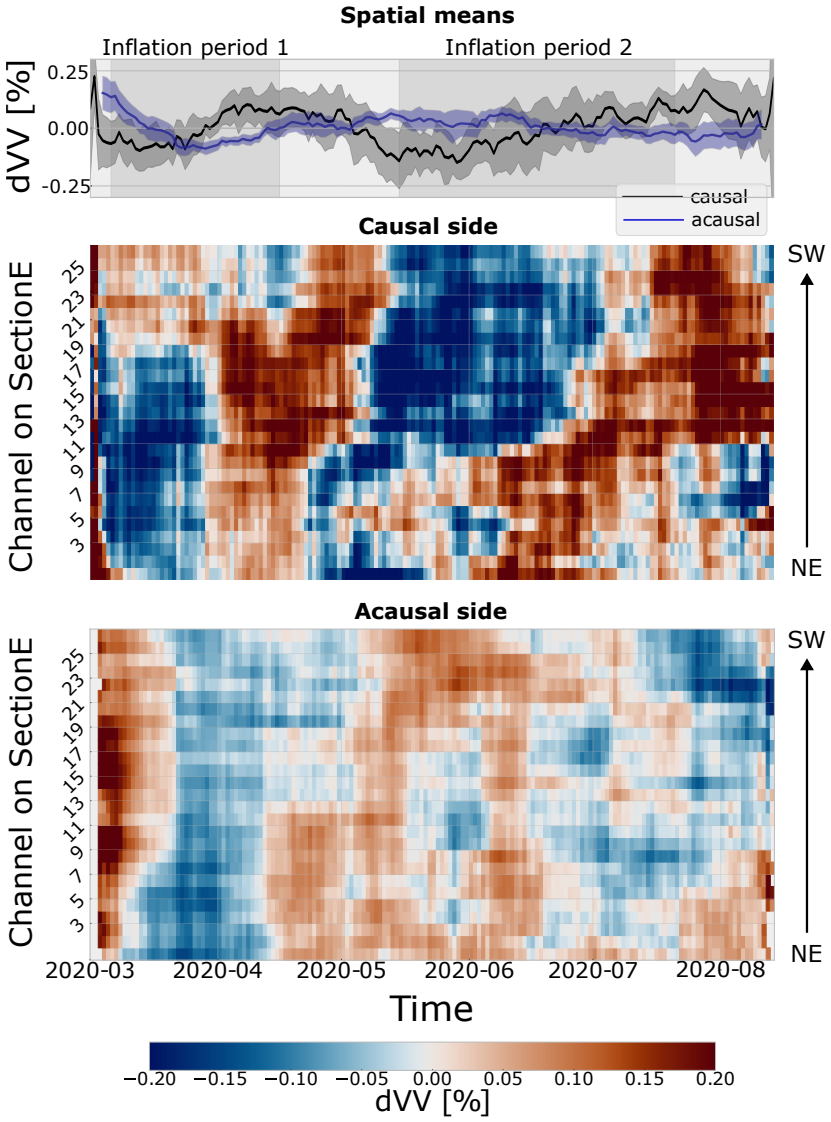

Figure 8: Comparison between acausal and causal side. Means over all (twenty-eight) gathers are displayed for a spatial stack length of $L = 200\,\mathrm{m}$. Spatially averaged velocity changes with standard deviations are displayed for causal and acausal sides at the top. Inflation periods are shaded with grey color. Contradicting, but spatially coherent velocity changes are measured on both sides of the cross-correlations.

6.4. Correlation with deformation and associated processes

We compare the averaged results to ground deformation and associated seismicity (Figure 9 and Figure S4). GPS data are from station SKSH which is located in the geothermal area close to SectionE (Figure 1). Constant trends and values deviating more than two times the standard deviation from the mean were removed prior to display. Because of the divergence of the North-American and Eurasian plate, we remove linear trends from the horizontal components. During vertical crustal inflation, the ground in SectionE exhibits slight westward movement, whereas it moves towards the east during subsidence. Negligible displacement is measured on the N-component. Except for the beginning of the analysed time period, spatially averaged velocity changes are positively correlated with the Z-component and the W-component of the GPS instrument. We exclude the possibility that changes in seismic velocities are caused by the static displacement. Measured velocity changes are of the order of 0.05%. Ground displacements observed at the GPS station are of the order of 5 mm horizontally and 8 cm vertically, which would result in length changes of the seismic raypath and thus, expected velocity changes of 0.00007% and 0.001%, calculated for the minimum distance of 7 km between virtual source and receiver. These values are three and one order of magnitude smaller than our measurements.

A link between vertical ground deformation in volcanic regions and changes of seismic velocities has been proposed in previous research. Numerous studies find a negative correlation between vertical ground motion and velocity changes (decreasing velocities during inflation). This has mostly been linked to magmatic intrusions, magma pressurization and associated open-

ing of cracks and fractures (e.g., Brenguier et al., 2008; Duputel et al., 2009; Mordret et al., 2010; Sens-Schönfelder et al., 2014; Bennington et al., 2015; Cubuk-Sabuncu et al., 2021). Positive correlations (increasing velocities during inflation) were also found, for example prior to an eruption at Merapi volcano (Ratdomopurbo and Poupinet, 1995) and at Kilauea volcano (Donaldson et al., 2017), and related to compression of the edifice caused by magma pressurization and closure of cracks. Thus, the same geological mechanisms have been invoked for interpretation of opposing measurements of velocity variations, and the subsurface geology, e.g., the existence of fissures and faults as well as the porosity and compressibility of rocks greatly affects the nature of the correlation. Donaldson et al. (2017) emphasize the importance of the depth of the inflating source and the resulting distribution of compressional and extensional strain in the crust. If seismic waves are sensitive to an area that undergoes extensional strain, a negative correlation between vertical ground deformation and velocity changes would be expected, and vice versa.

Cubuk-Sabuncu et al. (2021) also infer velocity changes in Reykjanes during the unrest period by applying coda wave interferometry to broadband seismic stations. They detect net decreased velocities between January and August of 2020 across different frequency ranges and relate this to repeated magmatic intrusions at $\approx 4\,\mathrm{km}$ depth and the concurrent opening of cracks. However, the authors analyze a much longer time period (up to ≈ 3 years) which also covers 'quiet' times without deformation, while our entire analysis time period (5.5 months) falls into the unrest period of 2020. Thus, a comparison of the studies is challenging as our dataset doesn't provide the temporal resolution necessary to compare seismic velocities during the unrest

period to seismic velocities during quieter times. Interestingly, the authors find that stations in the north-east of the inflating region measure a decrease in velocity prior to stations in the west of the inflating zone. The tendency for velocity changes to be measured first in the east and then in the west is generally consistent with our observations.

Flovenz et al. (2022) propose a model for the observed deformation in Reykjanes, in which each inflation period is caused by the intrusion of magmatic fluids into an aquifer at approximately 4 km depth. The aquifer resembles the approximate shape and location of the geothermal field outlined in Figure 1. The fluids are assumed to originate from a deeper sub-crustal source of melt east of the geothermal area and migrate along the brittle-ductile-boundary into the aquifer from the east to the west. Crustal inflation starts as the fluids reach the aquifer and create an overpressure large enough to lift the crust above it. We investigate whether our results could be associated with the fluid infiltration into the aquifer. Previous research indicates that seismic waves in our used frequency range (0.5 Hz to 0.9 Hz) and study area are particularly sensitive to structure in the upper few kilometers of the crust (Weemstra et al., 2016; Cubuk-Sabuncu et al., 2021) and may thus be affected by the fluid infiltration. Hence, the positive correlation between vertical ground motion and velocity changes could be associated with compression of the edifice caused by intruding fluids and closure of cracks. As fluids recede during crustal deflation, the crust relaxes, causing a decrease of wave velocities.

Velocity changes are also correlated with the W-component of the GPS-instrument (Figure 9a)). Generally, velocities increase as the ground moves to

the west, and decrease, as the ground moves to the east. For the first inflation period, there is a slight mismatch in time between dVV measurements and GPS data: while the ground starts to move towards the west at the beginning, the onset of the velocity increase is in the middle of the first inflation period. Discrepancies in timing between velocity changes and ground displacement could arise from the fact that we average velocity variations over both SectionE and SectionW. Consequently, our measurements encompass different geological conditions, such as fluid saturation and stress distribution in the crust, captured by all channels across the 1.2 km-long fiber segments. This may lead to differences compared to the GPS instrument, which only provides a single-point measurement of ground displacement, and to imperfect correlations between ground displacement and velocity changes. However, we note that the discrepancy is much less pronounced on measurements obtained for the causal sides of cross-correlations (Figure S5), indicating a possible connection with the contradictory measurements on causal and acausal sides as discussed in the previous section.

The link between velocity changes and horizontal ground deformation may again be associated with the infiltration of fluids from the northwest to the southeast at a depth of $\approx 4\,\mathrm{km}$, inducing pressurization and stress transfer within the subsurface during inflation, followed by crustal relaxation during deflation as the fluids retreat. However, the fact that DAS measures along the axial direction of the fiber (e.g., Martin et al., 2021), which in our case implies that it is particularly sensitive to variations in strain in the NE-SW direction, could contribute to our observations. We conclude that we can not yet provide a solid explanation for the correlation between our

measurements and the W-component of the GPS instrument. If and how the directivity of DAS affects the measurements would have to be investigated in future research.

We also explore a potential link between our findings and the spatio-temporal distribution of seismicity with a particular focus on our observation that velocity changes are first picked up by channels in the north-east and later in the south-west. During the analysed time period, more than 20,000 local earthquakes occurred in our study area. Seismic activity intensifies during crustal inflation and diminishes during deflation (Figure 9c) and d)). Depths range between several meters and 10 km, with most events being shallower than 5 km. Events are particularly shallow beneath the geothermal field where the brittle-ductile boundary domes up and deeper further away from it (Flovenz et al., 2022). We find no evidence of an initial occurrence of earthquakes further in the east followed by a subsequent westward progression over time, however, we cannot rule out that seismicity affects our measurements.

Overall, our results suggest a strong link between unrest periods in Reykjanes from March to mid-August of 2020 and seismic velocity changes. Ground deformation, fluid intrusions and local seismicity influence the stress distribution in the upper few kilometres of the crust during our time period. However, associating measured velocity changes with a specific geological mechanism is challenging, because all these processes happen at the same time and influence the measurements in possibly opposite ways. Also, the fact that different measurements are obtained for causal and acausal sides of cross-correlations (Section 6.3) suggests that the noise-source distribution affects

our measurements, and that the results may not be solely be attributable to structural changes in the crust. This raises the question to what extent our measurements can be interpreted geologically.

Even though not fully understood, our results demonstrate the potential of spatial stacking to improve the spatial coherency of velocity variations and increase their time resolution. With the applied technique, we were able to find a strong correlation between velocity variations and ground deformation at time scales that would not have been achievable with the classical workflow where no spatial stacking is applied. This motivates to further explore the power of DAS - its high spatial sampling - to enhance existing processing techniques and strategies for monitoring.

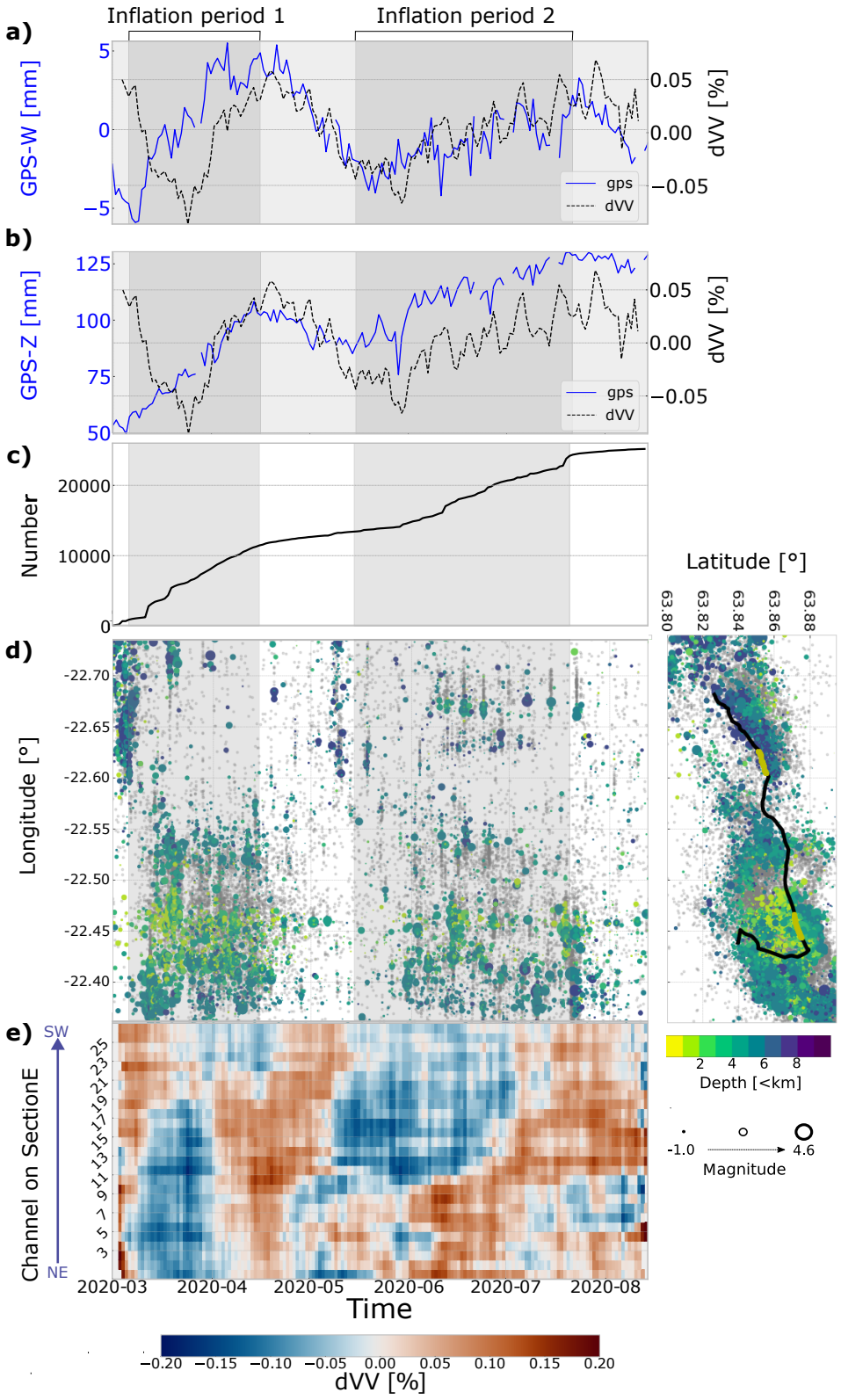

Figure 9: Geological interpretation of the results. On the x-axes, time is shown. Inflation periods are shaded with grey color. a) and b) Comparison between measurements and GPS data (W-, and Z-component). Standard deviations are not plotted for better visual comparison. c) and d) Cumulative number of earthquakes and spatio-temporal evolution of seismicity. Earthquake data are from two independent catalogues: events from the IMO catalogue are plotted in color with depths and magnitudes, events from the GFZ catalogue (Heimann et al., 2021), which captures a higher number of events but no magnitudes, in the background. The cumulative number is derived from the GFZ catalogue.

7. Conclusions and Implications

In this study, we combined ambient noise interferometry and DAS to monitor velocity variations in Reykjanes, south-west Iceland, between March 1 and August 14 of 2020. During this period of time, two inflation episodes of the crust, each followed by deflation, were observed. Using a methodological approach, we systematically explored what DAS adds as new contribution to seismic monitoring studies due to its high spatial resolution. We then investigated the link between geological processes and estimated temporal seismic velocity changes. Finally, we answer the questions posed in the introduction (Section 1).

How can we exploit the spatial resolution of DAS to improve coda wave interferometry?

We developed a new workflow based on spatial stacking of the raw data prior to cross-correlation, which affects measurements of relative velocity variations in two ways: (i) Time resolution is gained, which makes the measurements more sensitive to short-term environmental processes (Section 4). This confirms that DAS can detect structural and dynamic processes in the Earth that would not be identifiable with conventional datasets with comparatively sparse spatial sampling. (ii) Spatial stacking significantly improves the spatial and temporal coherency of the measurements, enabling us to reliably track changes in the sub-surface in time and space (Section 5). These findings have implications for various fields of research, such as the monitoring of ground water flow, magmatic intrusions and human infrastructure. They may help improve our understanding of stress transfer in the Earth and our ability to assess risks in hazardous areas. Finally, we emphasize that

spatial stacking of the raw data efficiently reduces the computational cost in noise-based interferometric studies, as the number of cross-correlations to be computed usually scales with the square of the number of involved traces. By stacking spatially prior to cross-correlation, the information about the wavefield contained in each trace further contributes to the analysis, which is in contrast to discarding traces, which carries the risk of losing valuable information.

Do measurements of seismic velocity variations correlate with the deformation between March and August of 2020 or associated processes?

Measured velocity changes correlate positively with ground displacement in both W- and Z-direction. This suggests a strong link between our measurements and the deformation. Overall, seismic velocities tend to be first picked up by channels in the north-east and at later times by channels in the south-west. Our results may be associated with pressure changes at depth and an associated redistribution of stress in the crust, induced by the northeast-southwestwards directed propagation of fluids at 4 km depth. However, it was found to be difficult to establish a causal relationship between our findings and a specific geological process. Situated atop the spreading mid-ocean ridge, the DAS cable occupies a volcanic zone characterized by a complex tectonic and geologic environment. Within this setting, various phenomena such as seismic activity, the migration of fluids, crustal deformation and the presence of high-temperature geothermal areas all influence the waveforms simultaneously and in different ways. What ultimately defines the nature of the correlation between ground deformation and seismic velocity

changes also depends on the geology of the subsurface and its response to the complex interaction of concurrent mechanisms.

In addition, different measurements are obtained for the causal and the acausal sides of cross-correlations which suggests that our measurements may not be based on fully scattered wavefields. While measured velocity changes are larger in magnitude for the causal sides and thus mainly make up for the trends observed in the averaged results, measurements on the acausal sides seem to show the opposite trend and thus anti-correlate with ground deformation in the Z- and the W-direction. This suggests that a quantitative geological interpretation might currently be constrained by conceptual limitations that need to be confronted in the future.

Overall, our observations not only showcase the capacity of DAS to unveil Earth processes at unprecedented resolution, but also to disclose and better understand limitations associated with current seismological methods. In future research, this knowledge will contribute to the enhancement of existing methods and ultimately help to improve our understanding of the Earth system's dynamic processes.

Open Research

The GFZ earthquake catalogue presented in this research is freely available (Heimann et al., 2021). Seismic data are provided by the GFZ Potsdam and are available in the GEOFON repository (Jousset et al., 2020). GPS data were downloaded from the open database of the IMO (Icelandic Met Office, 2024). Cross-correlations were computed with a self-modified version of the Python program "Noisepy" (Jiang and Denolle, 2020).

Acknowledgements

We are grateful to Egill Árni Guðnason and Þorbjörg Ágústsdóttir for helpful discussions about the Reykjanes peninsula and geothermal fields. We thank Christopher Wollin for providing the GFZ earthquake catalogue. We acknowledge support from the Emmy Noether program (HA7019/11) of the German Research Foundation (DFG), and from the European Union's Horizon 2020 research and innovation programme under the Marie Skłodowska-Curie grant agreement No 955515 – SPIN ITN (www.spin-itn.eu) and grant agreement No 858092- IMPROVE (www.improve-etn.eu).

Bibliography

Baisch, S., Bokelmann, G., 2001. Seismic waveform attributes before and after the Loma Prieta earthquake: Scattering change near the earthquake and temporal recovery. Journal of Geophysical Research 106, 16323–16337. URL https://doi.org/10.1029/2001JB000151

Bennington, N. L., Haney, M., De Angelis, S., Thurber, C. H., Freymueller, J., 2015. Monitoring changes in seismic velocity related to an ongoing rapid inflation event at okmok volcano, alaska. Journal of Geophysical Research: Solid Earth 120 (8), 5664–5676.
URL https://agupubs.onlinelibrary.wiley.com/doi/abs/10.1002/2015JB011939

Bensen, G. D., Ritzwoller, M. H., Barmin, M. P., Levshin, A. L., Lin, F., Moschetti, M. P., Shapiro, N. M., Yang, Y., 2007. Processing seismic ambient noise data to obtain reliable broad-band surface wave dispersion mea-

surements. Geophysical Journal International 169 (3), 1239–1260.
URL https://doi.org/10.1111/j.1365-246X.2007.03374.x

Bontemps, N., Lacroix, P., Larose, E., Jara, J., Taipe, E., 02 2020. Rain and small earthquakes maintain a slow-moving landslide in a persistent critical state. Nature Communications 11.
URL https://doi.org/10.1038/s41467-020-14445-3

Brenguier, F., Shapiro, N., Campillo, M., Ferrazzini, v., Duputel, Z., Coutant, O., Nercessian, A., 01 2008. Toward forecasting volcanic eruption using seismic noise. Nature geoscience 1.
URL https://doi.org/10.1038/ngeo104

Cheng, F., Ajo-Franklin, J. B., Nayak, A., Tribaldos, V. R., Mellors, R., Dobson, P., the Imperial Valley Dark Fiber Team, 2023. Using Dark Fiber and Distributed Acoustic Sensing to Characterize a Geothermal System in the Imperial Valley, Southern California. Journal of Geophysical Research: Solid Earth 128 (3), e2022JB025240.
URL https://doi.org/10.1029/2022JB025240

Chouet, B., 1979. Temporal variation in the attenuation of earthquake coda near Stone Canyon, California. Geophysical Research Letters 6 (3), 143–146.
URL https://doi.org/10.1029/GL006i003p00143

Colombi, A., Chaput, J., Brenguier, F., Hillers, G., Roux, P., Campillo, M., 2014. On the temporal stability of the coda of ambient noise correlations.

706 Comptes Rendus Geoscience 346 (11), 307–316.
707 URL https://doi.org/10.1016/j.crte.2014.10.002

708 Cubuk-Sabuncu, Y., Jónsdóttir, K., Caudron, C., Lecocq, T., Parks, M. M.,
709 Geirsson, H., Mordret, A., 2021. Temporal Seismic Velocity Changes Dur-
710 ing the 2020 Rapid Inflation at Mt. Þorbjörn-Svartsengi, Iceland, Using
711 Seismic Ambient Noise. Geophysical Research Letters 48 (11).
712 URL https://doi.org/10.1029/2020GL092265

713 Cupillard, P., Stehly, L., Romanowicz, B., 03 2011. The one-bit noise corre-
714 lation: a theory based on the concepts of coherent and incoherent noise.
715 Geophysical Journal International 184 (3), 1397–1414.
716 URL https://doi.org/10.1111/j.1365-246X.2010.04923.x

717 Czarny, R., Zhu, T., 2022. Estimating Rayleigh surface wave from ambient
718 noise recorded by distributed acoustic sensing (DAS) dark fiber array in
719 the city. pp. 2133–2137.
720 URL https://doi.org/10.1190/image2022-3750564.1

721 Diaz-Meza, S., Jousset, P., Currenti, G., Wollin, C., Krawczyk, C., Clarke,
722 A., Chalari, A., Apr 2023. On the Comparison of Records from Standard
723 and Engineered Fiber Optic Cables at Etna Volcano (Italy). Sensors 23 (7),
724 3735.
725 URL http://dx.doi.org/10.3390/s23073735

726 Donaldson, C., Caudron, C., Green, R. G., Thelen, W. A., White, R. S.,
727 2017. Relative seismic velocity variations correlate with deformation at

Kīlauea volcano. Science Advances 3 (6), e1700219.
URL https://doi.org/10.1126/sciadv.1700219

Dou, S., Lindsey, N., Wagner, A., Daley, T., Freifeld, B., Robertson, M., Peterson, J., Ulrich, C., Martin, E., Ajo-Franklin, J., 12 2017. Distributed Acoustic Sensing for Seismic Monitoring of The Near Surface: A Traffic-Noise Interferometry Case Study. Scientific Reports 7.
URL https://doi.org/10.1038/s41598-017-11986-4

Duputel, Z., Ferrazzini, V., Brenguier, F., Shapiro, N., Campillo, M., Nercessian, A., 2009. Real time monitoring of relative velocity changes using ambient seismic noise at the Piton de la Fournaise volcano (La Réunion) from January 2006 to June 2007. Journal of Volcanology and Geothermal Research 184 (1), 164–173.
URL https://doi.org/10.1016/j.jvolgeores.2008.11.024

Flovenz, O., Wang, R., Hersir, G., Dahm, T., Hainzl, S., Vassileva, M., Drouin, V., Heimann, S., Isken, M., Gudnason, E., Ágústsson, K., Agustsdottir, T., Horalek, J., Motagh, M., Walter, T. R., Rivalta, E., Jousset, P., Krawczyk, C., Milkereit, C., 2022. One year of cyclic unrest in a hydrothermal field as a harbinger of a volcanic eruption. Nature.
URL https://doi.org/10.21203/rs.3.rs-636186/v1

Froment, B., Campillo, M., Roux, P., Gouédard, P., Verdel, A., Weaver, R. L., 2010. Estimation of the effect of nonisotropically distributed energy on the apparent arrival time in correlations. GEOPHYSICS 75 (5), SA85–SA93.
URL https://doi.org/10.1190/1.3483102

752 Grêt, A., Snieder, R., Scales, J., 2006. Time-lapse monitoring of rock proper-
753 ties with coda wave interferometry. Journal of Geophysical Research: Solid
754 Earth 111 (B3).
755 URL https://doi.org/10.1029/2004JB003354

756 Guillemot, A., Helmstetter, A., Larose, E., Baillet, L., Garambois, S., May-
757 oraz, R., Delaloye, R., 03 2020. Seismic monitoring in the Gugla rock
758 glacier (Switzerland): ambient noise correlation, microseismicity and mod-
759 elling. Geophysical Journal International 221 (3), 1719–1735.
760 URL https://doi.org/10.1093/gji/ggaa097

761 Hadziioannou, C., Larose, É., Baig, A., Roux, P., Campillo, M., 2011. Im-
762 proving temporal resolution in ambient noise monitoring of seismic wave
763 speed. Journal of Geophysical Research.
764 URL https://doi.org/10.1029/2011JB008200

765 Hadziioannou, C., Larose, E., Coutant, O., Roux, P., Campillo, M., 06 2009.
766 Stability of monitoring weak changes in multiply scattering media with
767 ambient noise correlation: Laboratory experiments. The Journal of the
768 Acoustical Society of America 125 (6), 3688–3695.
769 URL https://doi.org/10.1121/1.3125345

770 Hartung, J., 2009. Lehr- und Handbuch der angewandten Statistik. Olden-
771 bourg Wissenschaftsverlag, München, pp. 1043–1150.
772 URL https://doi.org/10.1524/9783486710540.bm

773 Hasselmann, K., 1963. A statistical analysis of the generation of microseisms.

774 Reviews of Geophysics 1 (2), 177–210.
775 URL https://doi.org/10.1029/RG001i002p00177

776 Heimann, S., Isken, M. P., Dahm, T., 03 2021. Combining Horizontal Strain
777 DAS and Local Seismic Stations in a Full Waveform Attribute Stacking
778 Detector/Locator Algorithm: Verification Test for the Thorbjörn, Iceland,
779 2020 Unrest Episode [Dataset].
780 URL https://doi.org/10.5281/zenodo.6337788

781 Hillers, G., Campillo, M., Ma, K.-F., 2014. Seismic velocity variations at
782 TCDP are controlled by MJO driven precipitation pattern and high fluid
783 discharge properties. Earth and Planetary Science Letters 391, 121–127.
784 URL https://doi.org/10.1016/j.epsl.2014.01.040

785 Hirose, T., Nakahara, H., Nishimura, T., 2017. Combined use of repeated ac-
786 tive shots and ambient noise to detect temporal changes in seismic velocity:
787 application to Sakurajima volcano, Japan. Earth, Planets and Space 69,
788 1–12.
789 URL https://doi.org/10.1186/s40623-017-0613-7

790 Icelandic Met Office, 2024. GNSS Time-series station SKSH [Dataset]. On-
791 line; last accessed 3-April-2024.
792 URL https://brunnur.vedur.is/gps/browser/

793 Illien, L., Sens-Schönfelder, C., Andermann, C., Marc, O., Cook, K. L.,
794 Adhikari, L. B., Hovius, N., 2022. Seismic Velocity Recovery in the Sub-
795 surface: Transient Damage and Groundwater Drainage Following the 2015
796 Gorkha Earthquake, Nepal. Journal of Geophysical Research: Solid Earth

127 (2), e2021JB023402.
URL https://doi.org/10.1029/2021JB023402

Jiang, C., Denolle, M. A., 2020. NoisePy: A New High-Performance Python Tool for Ambient-Noise Seismology [Software]. Seismological Research Letters 91 (3), 1853–1866.
URL https://doi.org/10.1785/0220190364

Jousset, P., Currenti, G., Schwarz, B., Chalari, A., Tilmann, F., Reinsch, T., Zuccarello, L., Privitera, E., Krawczyk, C., 03 2022. Fibre optic distributed acoustic sensing of volcanic events. Nature Communications 13.
URL https://doi.org/10.1038/s41467-022-29184-w

Jousset, P., Hersir, G. P., Krawczyk, C., Wollin, C., Lipus, M., Reinsch, Thomas; Isken, M., Heimann, S., Maass, R., Schippkus, S., Hadziioannou, Céline, Schwarz, B., 2020. MAGIC (Magma Iceland). GFZ Data Services. [Other/Seismic Network].
URL https://doi.org/10.14470/0W7575244885

Jousset, P., Reinsch, T., Ryberg, T., Blanck, H., Clarke, A., Aghayev, R., Hersir, G. P., Henninges, J., Weber, M., Krawczyk, C. M., 2018. Dynamic strain determination using fibre-optic cables allows imaging of seismological and structural features. Nature Communications.
URL https://doi.org/10.1038/s41467-018-04860-y

Larose, E., Carrière, S., Voisin, C., Bottelin, P., Baillet, L., Guéguen, P., Walter, F., Jongmans, D., Guillier, B., Garambois, S., Gimbert, F., Massey, C., 2015. Environmental seismology: What can we learn on earth surface

processes with ambient noise? Journal of Applied Geophysics 116, 62–74.
URL https://doi.org/10.1016/j.jappgeo.2015.02.001

Larose, E., Roux, P., Campillo, M., Derode, A., 06 2008. Fluctuations of correlations and Green's function reconstruction: Role of scattering. Journal of Applied Physics 103 (11), 114907.
URL https://doi.org/10.1063/1.2939267

Li, Z., Shi, C., Ren, H., Chen, X., 2022. Multiple Leaking Mode Dispersion Observations and Applications From Ambient Noise Cross-Correlation in Oklahoma. Geophysical Research Letters 49 (1), e2021GL096032.
URL https://doi.org/10.1029/2021GL096032

Lin, F.-C., Tsai, V. C., Schmandt, B., Duputel, Z., Zhan, Z., 2013. Extracting seismic core phases with array interferometry. Geophysical Research Letters 40 (6), 1049–1053.
URL https://doi.org/10.1002/grl.50237

Lindsey, N. J., Dawe, T. C., Ajo-Franklin, J. B., 2019. Illuminating seafloor faults and ocean dynamics with dark fiber distributed acoustic sensing. Science 366 (6469), 1103–1107.
URL https://doi.org/10.1126/science.aay5881

Lindsey, N. J., Martin, E. R., 2021. Fiber-Optic Seismology. Annual Review of Earth and Planetary Sciences 49 (1), 309–336.
URL https://doi.org/10.1146/annurev-earth-072420-065213

Liu, Z., Huang, J., He, P., Qi, J., 2018. Ambient Noise Monitoring of Seismic Velocity Around the Longmenshan Fault Zone From 10 Years of Continu-

ous Observation. Journal of Geophysical Research: Solid Earth 123 (10), 8979–8994.
URL https://doi.org/10.1029/2018JB015986

Lobkis, O. I., Weaver, R. L., 2003. Coda-Wave Interferometry in Finite Solids: Recovery of P-to-S Conversion Rates in an Elastodynamic Billiard. Phys. Rev. Lett. 90.
URL https://doi.org/10.1103/PhysRevLett.90.254302

Longuet-Higgins, M. S., 1950. A Theory of the Origin of Microseisms. Philosophical Transactions of the Royal Society of London. Series A, Mathematical and Physical Sciences 243 (857).
URL https://doi.org/10.1098/rsta.1950.0012

Luo, B., Trainor-Guitton, W., Bozdağ, E., LaFlame, L., Cole, S., Karrenbach, M., 06 2020. Horizontally orthogonal distributed acoustic sensing array for earthquake- and ambient-noise-based multichannel analysis of surface waves. Geophysical Journal International 222 (3), 2147–2161.
URL https://doi.org/10.1093/gji/ggaa293

Mainsant, G., Larose, E., Brönnimann, C., Jongmans, D., Michoud, C., Jaboyedoff, M., 03 2012. Ambient seismic noise monitoring of a clay landslide: Toward failure prediction. Journal of Geophysical Research (Earth Surface) 117, 1030.
URL https://doi.org/10.1029/2011JF002159

Martin, E. R., Lindsey, N. J., Ajo-Franklin, J. B., Biondi, B. L., 2021. Introduction to Interferometry of Fiber-Optic Strain Measurements. American

866 Geophysical Union (AGU), Ch. 9, pp. 111–129.
867 URL https://doi.org/10.1002/9781119521808.ch9

868 Martins, J., Weemstra, C., Ruigrok, E., Verdel, A., Jousset, P., Hersir, G.,
869 2020. 3D S-wave velocity imaging of Reykjanes Peninsula high-enthalpy
870 geothermal fields with ambient-noise tomography. Journal of Volcanology
871 and Geothermal Research 391, 106685.
872 URL https://doi.org/10.1016/j.jvolgeores.2019.106685

873 Mordret, A., Jolly, A., Duputel, Z., Fournier, N., 2010. Monitoring of phreatic
874 eruptions using Interferometry on Retrieved Cross-Correlation Function
875 from Ambient Seismic Noise: Results from Mt. Ruapehu, New Zealand.
876 Journal of Volcanology and Geothermal Research 191 (1), 46–59.
877 URL https://doi.org/10.1016/j.jvolgeores.2010.01.010

878 Nakata, N., Chang, J. P., Lawrence, J. F., Boué, P., 2015. Body wave extrac-
879 tion and tomography at Long Beach, California, with ambient-noise inter-
880 ferometry. Journal of Geophysical Research: Solid Earth 120 (2), 1159–
881 1173.
882 URL https://doi.org/10.1002/2015JB011870

883 Obermann, A., Kraft, T., Larose, E., Wiemer, S., 2015. Potential of ambient
884 seismic noise techniques to monitor the St. Gallen geothermal site (Switzer-
885 land). Journal of Geophysical Research: Solid Earth 120 (6), 4301–4316.
886 URL https://doi.org/10.1002/2014JB011817

887 Obermann, A., Planès, T., Hadziioannou, C., Campillo, M., 07 2016. Lapse-
888 time-dependent coda-wave depth sensitivity to local velocity perturba-

tions in 3-D heterogeneous elastic media. Geophysical Journal International 207 (1), 59–66.
URL https://doi.org/10.1093/gji/ggw264

Parker, T., Shatalin, S., Farhadiroushan, M., 2014. Distributed Acoustic Sensing - A new tool for seismic applications. First Break 32.
URL https://doi.org/10.3997/1365-2397.2013034

Prieto, G. A., Denolle, M., Lawrence, J. F., Beroza, G. C., 2011. On amplitude information carried by the ambient seismic field. Comptes Rendus Geoscience 343 (8), 600–614.
URL https://doi.org/10.1016/j.crte.2011.03.006

Ratdomopurbo, A., Poupinet, G., 1995. Monitoring a temporal change of seismic velocity in a volcano: Application to the 1992 eruption of Mt. Merapi (Indonesia). Geophysical Research Letters 22 (7), 775–778.
URL https://doi.org/10.1029/95GL00302

Rodríguez Tribaldos, V., Ajo-Franklin, J. B., 2021. Aquifer Monitoring Using Ambient Seismic Noise Recorded With Distributed Acoustic Sensing (DAS) Deployed on Dark Fiber. Journal of Geophysical Research: Solid Earth 126 (4), e2020JB021004.
URL https://doi.org/10.1029/2020JB021004

Rost, S., Thomas, C., 2002. ARRAY SEISMOLOGY: METHODS AND APPLICATIONS. Reviews of Geophysics 40 (3).
URL https://doi.org/10.1029/2000RG000100

Schippkus, S., Safarkhani, M., Hadziioannou, C., Oct. 2023. Continuous isolated noise sources induce repeating waves in the coda of ambient noise correlations. Seismica 2 (2).
URL https://doi.org/10.26443/seismica.v2i2.499

Sens-Schönfelder, C., Pomponi, E., Peltier, A., 2014. Dynamics of Piton de la Fournaise volcano observed by passive image interferometry with multiple references. Journal of Volcanology and Geothermal Research 276, 32–45.
URL https://doi.org/10.1016/j.jvolgeores.2014.02.012

Shao, J., Wang, Y., Zheng, Y., Yao, Y., Wu, S., Yang, Z., Xue, Q., 2022. Near-surface characterization using urban traffic noise recorded by fiber-optic distributed acoustic sensing. Frontiers in Earth Science 10.
URL https://doi.org/10.3389/feart.2022.943424

Shragge, J., Yang, J., Issa, N., Roelens, M., Dentith, M., Schediwy, S., 03 2021. Low-frequency ambient distributed acoustic sensing (DAS): case study from Perth, Australia. Geophysical Journal International 226 (1), 564–581.
URL https://doi.org/10.1093/gji/ggab111

Snieder, R., Grêt, A., Douma, H., Scales, J., 2002. Coda wave interferometry for estimating nonlinear behavior in seismic velocity. Science 295 (5563), 2253–2255.
URL https://doi.org/10.1126/science.1070015

Snieder, R., Hagerty, M., 2004. Monitoring change in volcanic interiors using coda wave interferometry: Application to Arenal Volcano, Costa Rica.

Geophysical Research Letters 31 (9).
URL https://doi.org/10.1029/2004GL019670

Song, Z., Zeng, X., Chi, B., Bao, F., Osotuyi, A. G., Sep. 2022. Using the three-station interferometry method to improve urban DAS ambient noise tomography. Frontiers in Earth Science 10, 952410.
URL https://doi.org/10.3389/feart.2022.952410

Steinmann, R., Hadziioannou, C., Larose, E., 2020. Effect of centimetric freezing of the near subsurface on Rayleigh and Love wave velocity in ambient seismic noise correlations. Geophysical Journal International 224 (1), 626–636.
URL https://doi.org/10.1093/gji/ggaa406

Sánchez-Pastor, P., Obermann, A., Schimmel, M., Weemstra, C., Verdel, A., Jousset, P., 2019. Short- and Long-Term Variations in the Reykjanes Geothermal Reservoir From Seismic Noise Interferometry. Geophysical Research Letters 46 (11), 5788–5798.
URL https://doi.org/10.1029/2019GL082352

Toledo, T., Obermann, A., Verdel, A., Martins, J., Jousset, P., Mortensen, A., Erbas, K., Krawczyk, C., 2022. Ambient seismic noise monitoring and imaging at the Theistareykir geothermal field (Iceland). Journal of Volcanology and Geothermal Research 429, 107590.
URL https://doi.org/10.1016/j.jvolgeores.2022.107590

Tonegawa, T., Araki, E., Matsumoto, H., Kimura, T., Obana, K., Fujie, G., Arai, R., Shiraishi, K., Nakano, M., Nakamura, Y., Yokobiki, T.,

957 Kodaira, S., 2022. Extraction of P Wave From Ambient Seafloor Noise
958 Observed by Distributed Acoustic Sensing. Geophysical Research Letters
959 49 (4), e2022GL098162.
960 URL https://doi.org/10.1029/2022GL098162

961 Voisin, C., Garambois, S., Massey, C., Brossier, R., 2016. Seismic noise mon-
962 itoring of the water table in a deep-seated, slow-moving landslide. Inter-
963 pretation 4 (3), SJ67–SJ76.
964 URL https://doi.org/10.1190/INT-2016-0010.1

965 Wang, K., Luo, Y., Zhao, K., Zhang, L., 25(6) 2014. Body Waves Revealed
966 by Spatial Stacking on Long-Term Cross-Correlation of Ambient Noise.
967 Journal of Earth Science 7, 977–984.
968 URL https://doi.org/10.1007/s12583-014-0495-6

969 Wapenaar, K., Draganov, D., Snieder, R., Campman, X., Verdel, A., 2010.
970 Tutorial on seismic interferometry. Part I: Basic principles and applica-
971 tions. Geophysics 75, 75A195–75209.
972 URL https://doi.org/10.1190/1.3457445

973 Weemstra, K., Obermann, A., Verdel, A., Paap, B., Blanck, H., Guðnason,
974 E., Hersir, G., Jousset, P., Sigurðsson, Ö., 2016. Time-lapse seismic imag-
975 ing of the reykjanes geothermal reservoir. European Geothermal Congress
976 2016, EGC 2016 ; Conference date: 19-09-2016 Through 24-09-2016.
977 URL http://europeangeothermalcongress.eu/

978 Wegler, U., Sens-Schönfelder, C., 03 2007. Fault zone monitoring with passive
979 image interferometry. Geophysical Journal International 168 (3), 1029–

1033.
URL https://doi.org/10.1111/j.1365-246X.2006.03284.x

Williams, E., Fernandez-Ruiz, M. R., Magalhães, R., Vanthillo, R., Zhan, Z., Gonzalez-Herraez, M., Martins, H. F., 2019. Distributed sensing of microseisms and teleseisms with submarine dark fibers. Nature Communications 10 (1), 5778–5778.
URL https://doi.org/10.1038/s41467-019-13262-7

Zhan, Z., 2019. Distributed Acoustic Sensing Turns Fiber-Optic Cables into Sensitive Seismic Antennas. Seismological Research Letters 91 (1), 1–15.
URL https://doi.org/10.1785/0220190112

Zhou, W., Butcher, A., Brisbourne, A. M., Kufner, S.-K., Kendall, J.-M., Stork, A. L., 2022. Seismic Noise Interferometry and Distributed Acoustic Sensing (DAS): Inverting for the Firn Layer S-Velocity Structure on Rutford Ice Stream, Antarctica. Journal of Geophysical Research: Earth Surface 127 (12), e2022JF006917.
URL https://doi.org/10.1029/2022JF006917

Supporting Information for "Stacking of distributed dynamic strain reveals link between seismic velocity changes and the 2020 unrest in Reykjanes"

Regina Maass[1,2] *,Sven Schippkus [2], Céline Hadziioannou [2], Benjamin Schwarz [3,4], Philippe Jousset[3], Charlotte Krawczyk [3,5]

[1]University of Hamburg, Hamburg, Germany

[2]now at Dublin Institute for Advanced Studies, Dublin, Ireland

[3]GFZ German Research Centre for Geosciences, Potsdam, Germany

[4]Fraunhofer Institute for Wind Energy Systems IWES, Bremen, Germany

[5]Technical University Berlin, Berlin, Germany

Contents of this file

1. Text S1
2. Figures S1 to S5

Introduction

This supporting information provides Figures S1 to S5 as referenced in the main text. For data shown in Figure S1, processing is described in Text S1.

*Email, maass@cp.dias.ie

Text S1: Beamforming

Beamforming was applied to a separate dataset including every 50th channel along the 21-km long DAS cable and 30 days of data from March 2020. Empirical Green's functions were extracted using ambient noise interferometry. At first, a virtual source was selected. Then, daily cross-correlations between the virtual source and all other channels were computed in the frequency range 0.5 Hz - 0.9 Hz and subsequently stacked to increase the signal-to noise ratio (SNR) of cross-correlations. Results are displayed in the correlation gather in Figure S1a). Beamforming was applied to a subset of the data with good SNR (Figure S1b) and yields an apparent velocity of 1.93 km/s (Figure S1c).

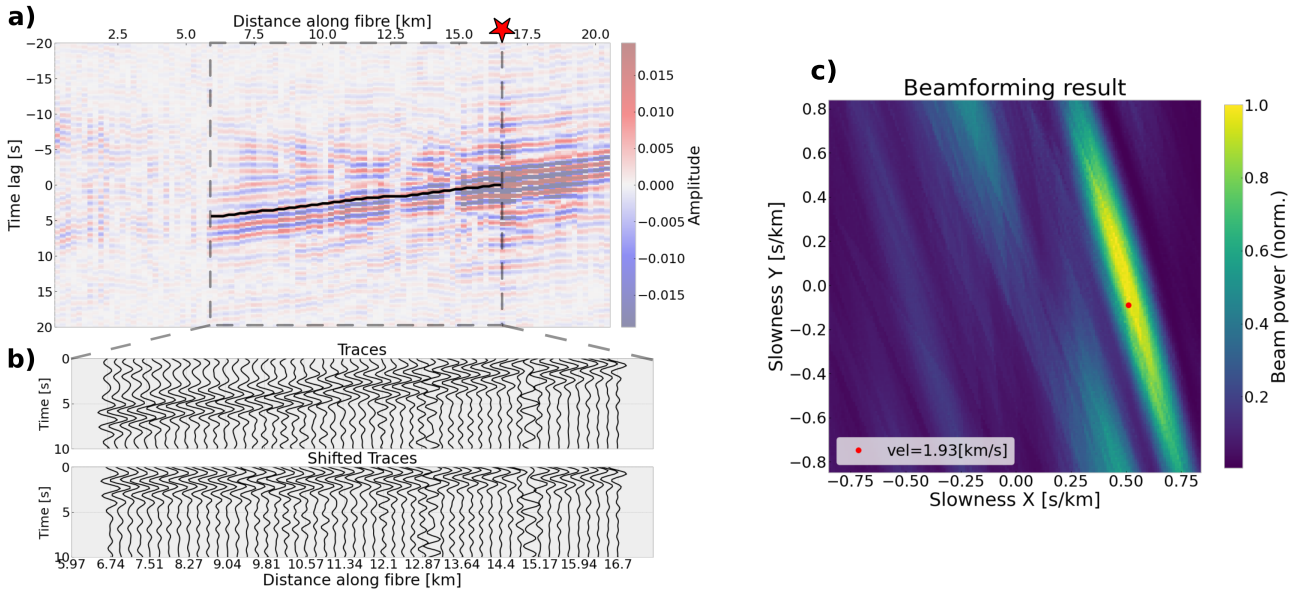

Figure S1. Beamforming. Data processing is described in Text S1. a) Correlation gather showing cross-correlations between the virtual source (red star) and all other stations. The subset used for beamforming is marked with the grey dashed line. The black line indicates the moveout corresponding to the best-fitting wave velocity 1.93 km/s obtained with beamforming. b) Wiggle traces for data subset marked in a) and traces after shifting them using the best-fitting velocity. c) Beamforming result. A grid search was applied to a reasonable range of slownesses in the X (longitude) and Y (latitude).

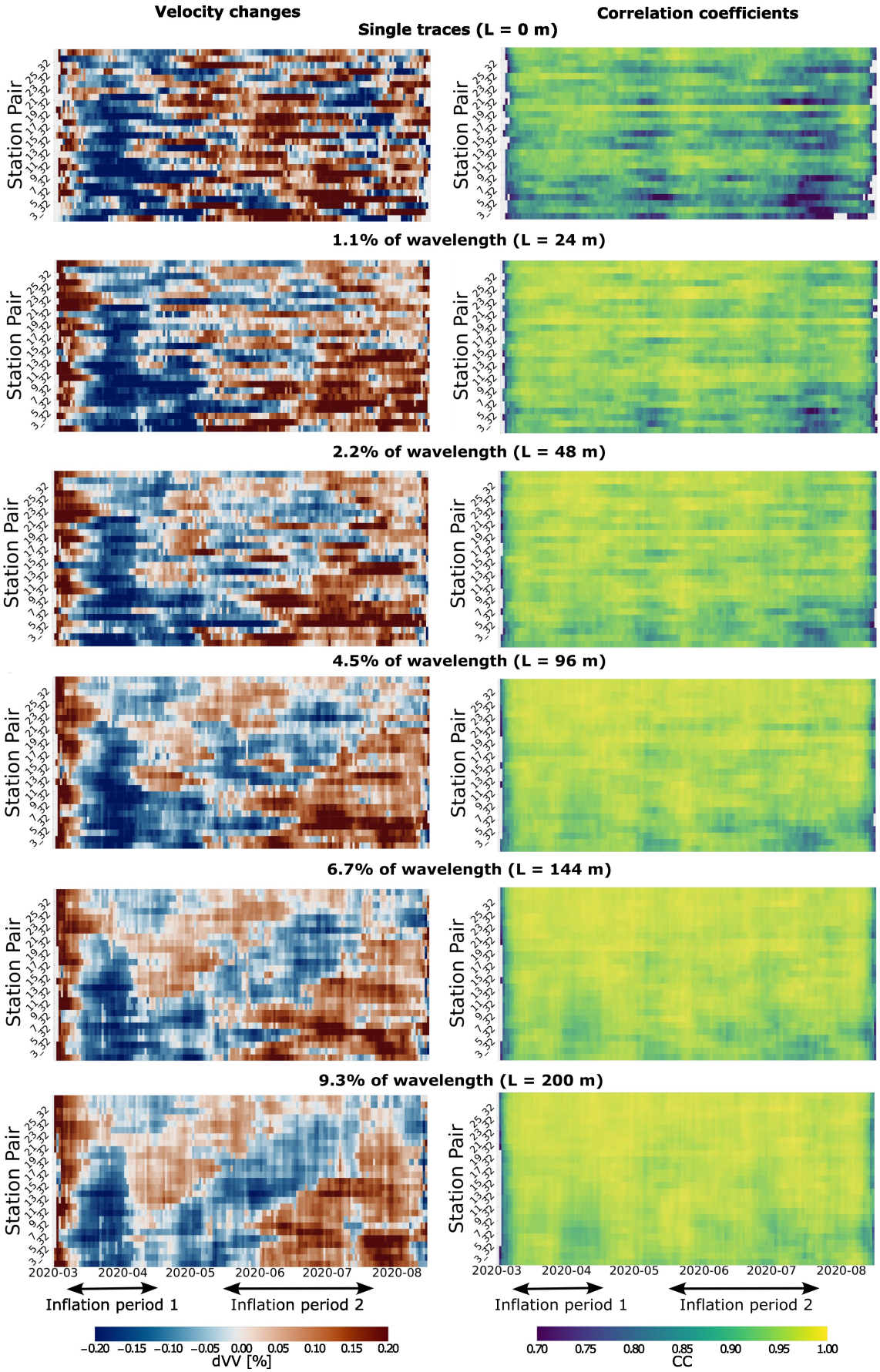

Figure S2. Gathers for an increasing spatial stack length L (reference channel 32). Figure caption as in Figure 6 in the main text.

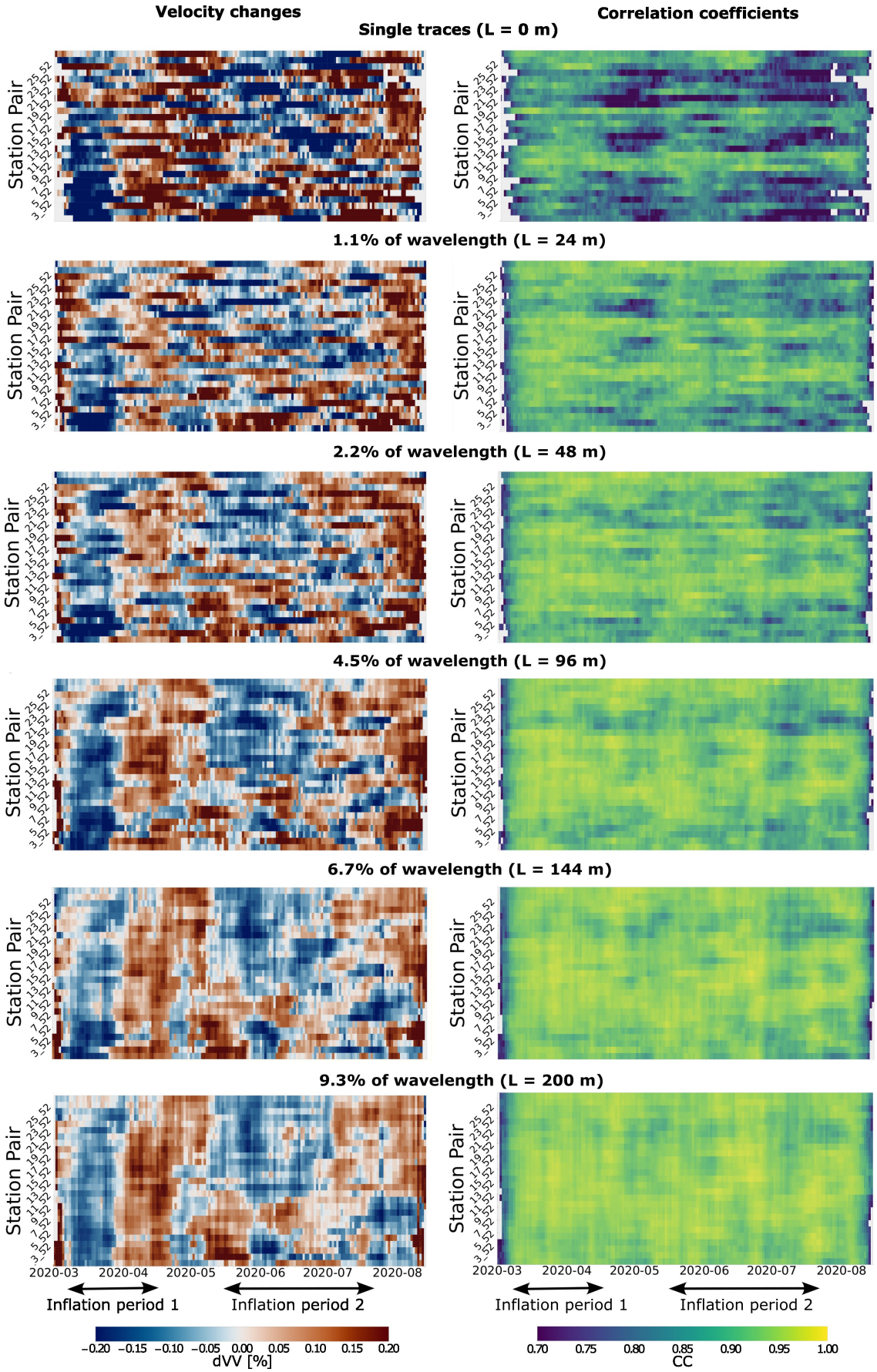

Figure S3. Gathers for an increasing spatial stack length L (reference channel 52). Figure caption as in Figure 6 in the main text.

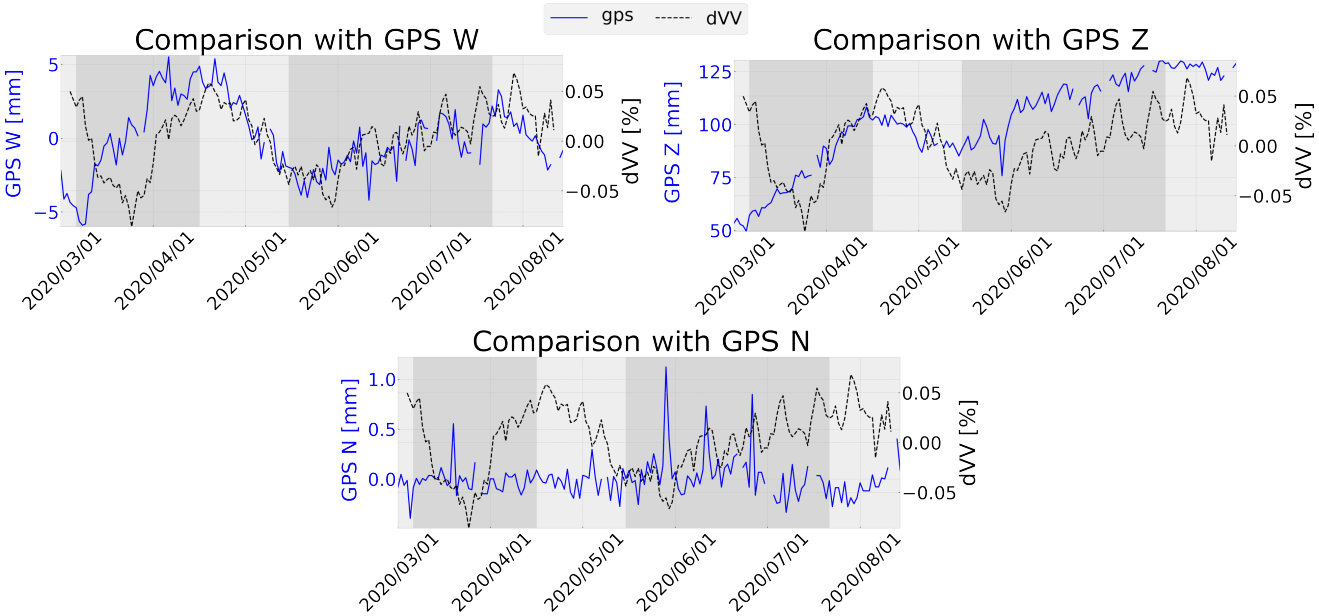

Figure S4. Comparison between ground deformation in Reykjanes (station SKSH, see Figure 1 in main text) and seismic velocity changes (dVV). Standard deviations are not plotted for better visual comparison. The west (W), vertical (Z) and north (N) components are shown.

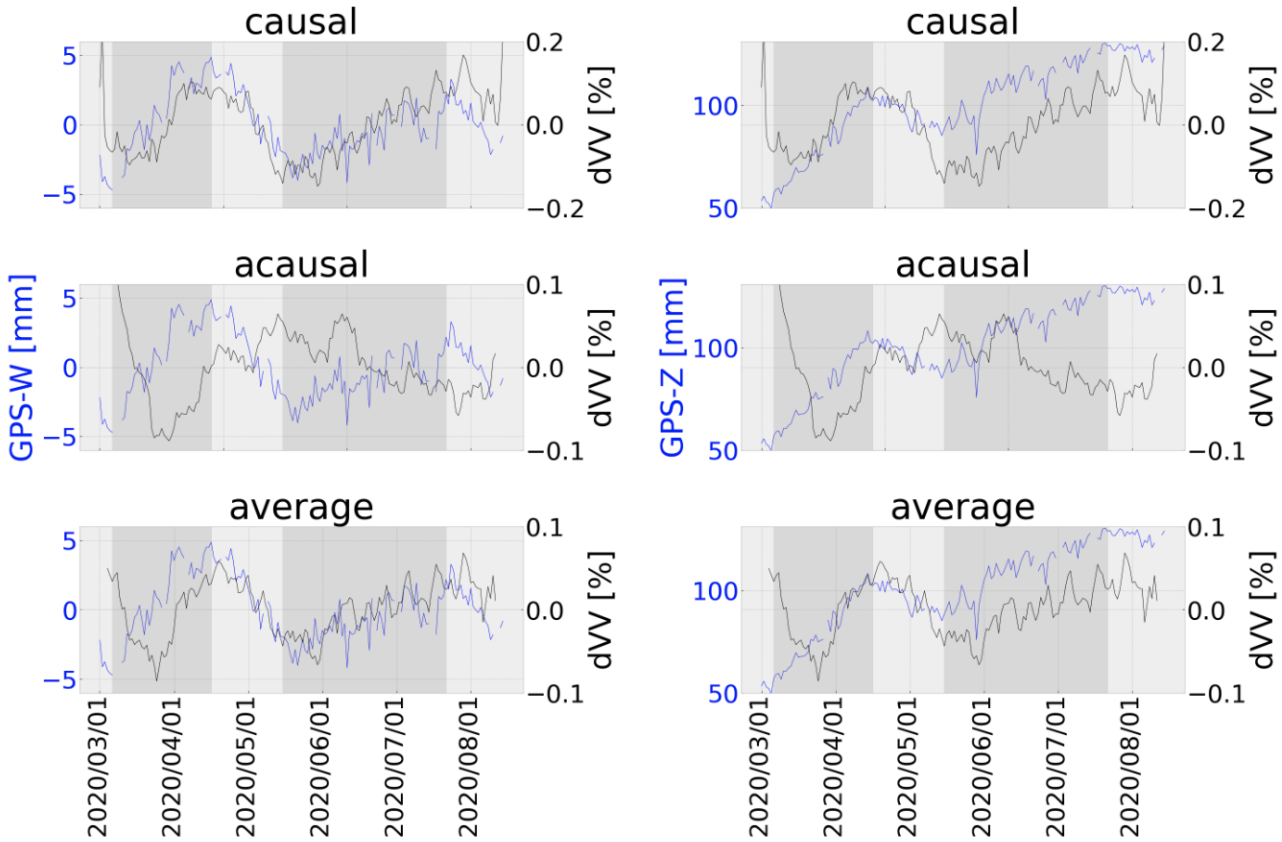

Figure S5. Comparison between vertical and horizontal (E-W) ground deformation in Reykjanes (station SKSH, see Figure 1 in main text) and seismic velocity changes (dVV), measured for causal and acausal sides of cross-correlations individually. Standard deviations are not plotted for better visual comparison.